

## RESEARCH ARTICLE

10.1002/2017JD026488

## Key Points:

- Spatial models of particles from focused ion beam tomography are highly useful for determining how shape and composition affect particle optical properties
- Regardless if absorption or scattering dominates, shape is more important for determining extinction than accounting for compositions of individual phases
- For particles with phases having widely varying refractive indexes, only models that account for composition heterogeneity may sufficiently determine albedo

## Supporting Information:

- Supporting Information S1

## Correspondence to:

J. M. Conny,  
joseph.conny@nist.gov

## Citation:

Conny, J. M., and D. L. Ortiz-Montalvo (2017), Effect of heterogeneity and shape on optical properties of urban dust based on three-dimensional modeling of individual particles, *J. Geophys. Res. Atmos.*, 122, doi:10.1002/2017JD026488.

Received 12 JAN 2017

Accepted 17 AUG 2017

Accepted article online 24 AUG 2017

Published 2017. This article is a U.S. Government work and is in the public domain in the USA.

## Effect of heterogeneity and shape on optical properties of urban dust based on three-dimensional modeling of individual particles

Joseph M. Conny<sup>1</sup>  and Diana L. Ortiz-Montalvo<sup>1</sup> 

<sup>1</sup>Materials Measurement Science Division, National Institute of Standards and Technology, Gaithersburg, Maryland, USA

**Abstract** We show the effect of composition heterogeneity and shape on the optical properties of urban dust particles based on the three-dimensional spatial and optical modeling of individual particles. Using scanning electron microscopy/energy-dispersive X-ray spectroscopy (SEM/EDX) and focused ion beam (FIB) tomography, spatial models of particles collected in Los Angeles and Seattle accounted for surface features, inclusions, and voids, as well as overall composition and shape. Using voxel data from the spatial models and the discrete dipole approximation method, we report extinction efficiency, asymmetry parameter, and single-scattering albedo (SSA). Test models of the particles involved (1) the particle's actual morphology as a single homogeneous phase and (2) simple geometric shapes (spheres, cubes, and tetrahedra) depicting composition homogeneity or heterogeneity (with multiple spheres). Test models were compared with a reference model, which included the particle's actual morphology and heterogeneity based on SEM/EDX and FIB tomography. Results show particle shape to be a more important factor for determining extinction efficiency than accounting for individual phases in a particle, regardless of whether absorption or scattering dominated. In addition to homogeneous models with the particles' actual morphology, tetrahedral geometric models provided better extinction accuracy than spherical or cubic models. For iron-containing heterogeneous particles, the asymmetry parameter and SSA varied with the composition of the iron-containing phase, even if the phase was <10% of the particle volume. For particles containing loosely held phases with widely varying refractive indexes (i.e., exhibiting "severe" heterogeneity), only models that account for heterogeneity may sufficiently determine SSA.

### 1. Introduction

Atmospheric dust aerosols affect climate by perturbing Earth's radiative balance directly or through aerosol interaction with clouds [Haywood and Boucher, 2000; Satheesh and Krishna Moorthy, 2005; Sokolik and Toon, 1996]. For effects involving clouds, known collectively as indirect aerosol effects or aerosol-cloud interactions, the size and composition of dust particles as cloud droplet condensation nuclei or ice nuclei affect the physical properties of cloud droplets or ice crystals and the overall optical thickness, albedo, and lifetime of clouds [Albrecht, 1989; Haywood and Boucher, 2000; Lohmann and Feichter, 2005; Myhre et al., 2013; Twomey, 1974]. In addition, absorbing aerosol in the vicinity of clouds may warm the atmosphere and reduce cloud cover (semidirect effect) [Hansen et al., 1997].

The direct aerosol effect is the scattering or absorption of solar or longwave radiation by aerosol particles without cloud interaction [Haywood and Boucher, 2000; Myhre, 2009]. The imbalance in Earth's radiative flux due to the direct effect, quantified as radiative forcing in watts per meter squared at the top of the atmosphere (TOA), is calculated from properties that can be assigned to aerosol particles: extinction coefficient, single-scattering albedo (SSA—ratio of scattering to extinction), and asymmetry parameter (average cosine of the scattering angle) or phase function (fractions of light scattered in particular directions). The aerosol optical depth (AOD) is calculated from the particle extinction coefficient. The extent of aerosol scattering versus absorption is derived from the SSA. The extent that radiation is backscattered is derived from the asymmetry parameter or phase function.

Atmospheric dust is often assumed to be mineral in origin such as the large injections of dust from major desert regions such as the Sahara, Gobi, and Taklamakan. Radiative forcing by dust has been assumed to be negative in the solar spectrum and positive in the thermal infrared spectrum [Teegen et al., 1996], notwithstanding variation in forcing due to the surface albedo, e.g., land versus ocean. Local TOA variation in

radiative forcing (solar plus infrared) from dust due to disturbed soils from anthropogenic activities ranges from  $-2.1$  to  $5.5 \text{ W m}^{-2}$  [Tegen et al., 1996].

Dust of urban origin (exclusive of solitary soot-like or sulfate particles) has signatures that are both mineral and uniquely anthropogenic such as cement, masonry and asphalt wear, tire wear, demolition dust, and emissions from power plants and energy intensive manufacturing [Conny and Norris, 2011; Sokolik and Toon, 1996]. Mineral dust from human activities alone is thought to contribute 20 to 50% of the global mineral dust loading [Sokolik and Toon, 1996; Tegen and Fung, 1995]. While mineral particles themselves often exhibit composition heterogeneity [Falkovich et al., 2001; Nousiainen, 2009; Toon and Pollack, 1976], individual urban particles often exhibit the mixing of nonmineral components such as soot or sulfate with mineral components [Conny and Norris, 2011], similar to the “aging” of aerosols in nonurban environments [Buseck and Posfai, 1999; Levin et al., 1996].

In this work, we model the optical properties of selected individual urban dust particles and account for their composition heterogeneity and morphology (surface features and void structure as well as shape). In addition, we present optical models of the particles with lesser complexity. One type of simplified model includes the actual size and morphology of the particle, but with its composition as a single homogeneous phase. Other simplified models are volume-equivalent geometric shapes consisting of a single cube, tetrahedron, sphere, or multiple spheres. We compare optical properties of the simplified models (test models) of a particle with a reference model representing the actual morphology and composition of the particle to show how shape and heterogeneity affect optical behavior of urban dust.

The reference models in this study are derived from the detailed spatial analysis of each particle with focused ion beam scanning electron microscopy (FIB-SEM) and associated element mapping by energy-dispersive X-ray spectroscopy (EDX). SEM and/or transmission electron microscopy have been employed in a number of studies on the optical properties of dust aerosols [e.g., Ebert et al., 2004, 2002; Kalashnikova and Sokolik, 2004; Kandler et al., 2007, 2009]. However, few reports on the use of FIB-SEM on atmospheric particles are known [Adler et al., 2014; Chen et al., 2013; Conny, 2013; Conny et al., 2014; Lieke et al., 2013]. This study contrasts with previous studies involving SEM, EDX, and FIB-SEM in that we investigate particle optical behavior based on the three-dimensional internal structure and composition of particles and overall particle morphology with a technique known as FIB tomography [Conny et al., 2014].

Dust particles rarely have shapes that closely match simple geometric forms [Gao and Anderson, 2001; Kalashnikova and Sokolik, 2002; Nousiainen, 2009; Volten et al., 2001]. However, algorithms that retrieve aerosol optical properties from satellite-based instruments such as MODIS (Moderate Resolution Imaging Spectroradiometer) and MISR (Multiangle Imaging Spectroradiometer) [Diner et al., 1999; King et al., 1999; Remer et al., 2005] or ground-based radiometers within AERONET (Aerosol Robotics Network) [Holben et al., 1998] necessarily approximate particles as homogeneous geometric forms, typically spheres or spheroids. Significant deviation in the scattering phase function from purely spherical models has been shown for non-spherical particle models consisting of spheroids (oblate and prolate) and Chebyshev forms [Asano and Sato, 1980; Hill et al., 1984; Kahnert and Kylling, 2004; Koepke and Hess, 1988; Mishchenko et al., 1995, 1997; Wiscombe and Mugnai, 1988; Yi et al., 2011] and for more realistic particle shapes based on electron microscopy [Kalashnikova and Sokolik, 2002, 2004]. As a result, AOD retrievals from satellite and ground-based radiometers have been shown to be inaccurate especially when only spherically shaped particles are considered [Dubovik et al., 2002, 2000; Kahn et al., 1997]. In this study, we assess how well optical models with simplified particle shapes compare with models that incorporate the morphology and internal structure of actual dust particles.

An important related problem is our ability to adequately characterize the shape and size of dust particles using measurement techniques such as conventional two-dimensional SEM, aerodynamic particle sizing, and optical particle sizing [Reid et al., 2003]. Various approaches have been taken to address shape-related inaccuracies in AOD retrievals [Dubovik et al., 2006; Kalashnikova and Kahn, 2006]. Relatively recent updates to AERONET and MODIS retrieval algorithms assigned spheres to fine-mode particles, which are assumed to be of anthropogenic and biomass burning origins, and randomly oriented spheroids to coarse-mode mineral dust particles [Dubovik et al., 2006; Levy et al., 2007]. Radiometric spectral information has also been used to distinguish particle sphericity from nonsphericity with modeled spheroids having a distribution of aspect ratios [Dubovik et al., 2006; Kahn et al., 1997] and as aggregates of simple geometric forms [Kalashnikova and Kahn, 2006].

Due to the complexity of heterogeneous particles and the limitation of EDX to elemental rather than chemical species analysis, the identity of individual phases is often ambiguous. For a small number of particles (seven), we consider different compositions for the light-absorbing phase such as elemental carbon and various iron oxides within each particle for a total of 18 model treatments. In particular, elemental carbon phases are modeled as soot-like black carbon or graphite; iron-containing phases are modeled as hematite, goethite, limonite, wustite, or a nonabsorbing iron-containing silicate. From the 3-D spatial models with FIB tomography, we calculate extinction, absorption, and scattering efficiencies and asymmetry parameters for the model treatments using the discrete dipole approximation (DDA) method [Draine and Flatau, 1994; Yurkin and Hoekstra, 2007, 2016], known also as the coupled dipole approximation. We focus on the variation in extinction, SSA, and the asymmetry parameter between the test and reference models.

## 2. Methodology

### 2.1. Sample Collection and Preparation

Particles in approximately the 2.5 to 10  $\mu\text{m}$  size range were collected at sampling sites in Los Angeles (LA) in fall 2004 and Seattle in winter 2005. At each site, particles were collected on a quartz-fiber filter using a dichotomous virtual impactor (Universal Air Sampler, MSP Corporation) that ran continuously for 24 h. (Commercial products identified here specify the means by which experiments were conducted. Such identification is neither intended to imply recommendation or endorsement by the National Institute of Standards and Technology nor imply that the identified products are necessarily the best available for the purpose.) The LA sampling site (latitude 34.02°, longitude  $-118.28^\circ$ ) was located 4 km south of downtown in a light industrial area and approximately 150 m from a major highway. The sample likely contained significant amounts of particles originating from the nearby highway. The Seattle sampling site (latitude 47.71°, longitude  $-122.29^\circ$ ) was located in a recreational park adjacent to a residential neighborhood of detached homes, 9 km north of downtown and 2.9 km from a major highway. The sample likely contained significant amounts of mineral-like particles from the park and neighborhood grounds.

The seven selected particles ranged in size from 1.28 to 3.37  $\mu\text{m}$ . Dichotomous samplers of the type employed here typically have a 50% efficiency at the aerodynamic diameter cut point between the fine particle fraction (0 to 2.5  $\mu\text{m}$ ) and the coarse fraction (2.5 to 10  $\mu\text{m}$ ) [Hinds, 1999]. In this study, three particles had diameters below the 2.5  $\mu\text{m}$  cut point and four particles had diameters above the 2.5  $\mu\text{m}$  cut point but at the lower end of the coarse particle size range. Thus, they were relatively small dust particles.

### 2.2. EDS Analysis and FIB Tomography

FIB tomography is performed with an SEM instrument that has an ion beam column in addition to the electron beam column. The process involves sequentially milling through the particle with the ion beam while collecting SEM images. In addition, mapping of elements by EDX determines the compositional heterogeneity. The images and maps are used to provide a 3-D reconstruction of the particle's shape, surface features, and internal structure and composition. Voxel positions from the 3-D spatial models are then used as input to DDA for creating optical models.

Particles were transferred from the quartz-fiber filters to 5 mm  $\times$  5 mm germanium wafers using an electrostatically assisted microcentrifugation technique [Conny *et al.*, 2014]. Prior to imaging and EDX element mapping in the SEM, particle-borne wafers were coated with 10 to 20 nm of carbon to minimize charging by the electron beam. Secondary electron imaging, element mapping and analysis by EDX, and FIB tomography of the particles were performed with an FEI Nova NanoLab 600 Dual-Beam (electron and gallium-ion beams). The electron beam energy and current were 15 kV and 0.58 nA or 20 kV and 0.62 nA. Element compositions were determined from EDX maps of the whole particle or subregions of the particle, thus excluding the surrounding wafer.

The FIB-SEM instrument stage is tilted 52° such that the  $\text{Ga}^+$  ion beam is normal to the substrate, but the electron beam is 52° from the normal (38° from the wafer surface) [Conny, 2013] (see Figure S1 in the supporting information). An automated process mills through the particle in 15 to 20 nm increments and then images the particle's exposed surface. The result is a stack of 100 to 200 images with 1024 by 884 pixels for each particle. In this study, pixel sizes ranged from 4.8 to 15.6 nm. For some particles, element maps with EDX

were taken at every tenth slice. In most cases using germanium substrates, overlap of Ge  $L$  X-ray lines from the substrate with  $K$  lines from sodium and magnesium in the particle precluded the analysis of Na and Mg. However, Na and Mg are sometimes detectable from a surface inclusion when the underlying particle sufficiently absorbs the interfering Ge  $L$  X-rays. Na and Mg are also detectable when maps are taken with the electron beam at  $52^\circ$  from the normal, whereby the beam penetrates less of the wafer and fewer Ge  $L$  X-rays reach the EDX detector.

The 3-D representation of each particle was created from the stack of SEM images using Avizo software version 7. Using Avizo's manual segmentation tools, each voxel in the 3-D representation was assigned a chemical phase based on the EDX element maps. During FIB milling, slicing occurs in the  $z$  direction. However, the 15 to 20 nm FIB slice increment is larger than the size of an image pixel in the  $x$ - $y$  plane. As a result, voxels in the 3-D representation are not cubic initially. Resampling of the 3-D representation in Avizo was required to make the voxels as close to cubic as possible while maintaining the size, shape, and chemical phase assignment of the original 3-D representation.

### 2.3. Optical Property Modeling

Optical properties (extinction, absorption, scattering, and asymmetry parameter) were calculated for incident light at the 589 nm wavelength using the DDA program DDSCAT version 7.3 [Draine and Flatau, 1994, 2013]. (Note that 589 nm is the spectral D line of sodium used by convention for refractive index measurements.) The DDA method employs a user-specified set of points describing the particle whereby each point is a polarizability tensor, or dipole, subject to the electric field of the incident monochromatic light and the electric field of the other dipoles [Draine, 2000]. Using the appropriate sets of dipoles, DDA can accommodate a particle's exact shape, surface features, and void structure. Other numerical techniques for determining optical properties of nonspherical particles may also be suitable such as the invariant imbedding T-matrix method [Bi and Yang, 2014]. Some techniques are more appropriate for homogeneous particles or particle cluster components that have rotational symmetry, such as the separation of variables method, standard T-matrix method, and the superposition method for multisphere/spheroid clusters [Mishchenko *et al.*, 2000]. Other techniques such as the finite element, finite difference, or the finite difference time domain methods that allow for heterogeneity and asymmetry are limited by the particle size parameter (e.g.,  $x = 2\pi a/\lambda < 10$ , where  $\lambda$  is the wavelength of incident light and  $a$  is the particle size such as the radius of a volume-equivalent sphere) [Mishchenko *et al.*, 2000].

In DDSCAT, a target is defined as an array of points that are polarizable, i.e., array of dipoles, by incident light. For the shape and compositional structure of a particle, DDSCAT requires an input file with dipole  $x$ ,  $y$ , and  $z$  coordinates, whereby each dipole is associated with a complex refractive index. For each particle, the number of voxels in the 3-D representation exceeded the DDSCAT dipole capacity ( $10^6$ ). To provide DDSCAT with fewer dipoles, 3-D representations were necessarily downsampled in Avizo. Models of geometric forms of particles, as explained below, were generated from internal DDSCAT procedures rather than a file of dipole coordinates.

In this study, complex refractive indexes were acquired from various sources (see Tables 3 and 4 below). For the real part of the refractive index of mineral phases, we primarily used data from the *Handbook of Mineralogy* [Anthony *et al.*, 2016]. To maintain consistency among crystalline materials with uniaxial or biaxial birefringence, we selected the extraordinary or gamma refractive index component, respectively. For the imaginary part of the refractive index we used various literature values; most importantly, for minerals we used tabular data from Egan and Hilgeman [1979], which included data at 600 nm, the listing closest to 589 nm. References for refractive indexes associated with specific particles and phases are listed in Tables 3 and 4.

To simulate random orientation of a particle in the atmosphere, the target is rotated in DDSCAT within a computational frame (lab frame) at specified intervals [Draine and Flatau, 2013]. The lab frame is defined by axes  $\hat{x}$ ,  $\hat{y}$ , and  $\hat{z}$ , whereby incident light propagates along the  $\hat{x}$  axis and the two polarization states for the incident light align with the  $\hat{y}$  and  $\hat{z}$  axes. The target is oriented within the lab frame by its internal axes. Three angles are used to specify the target orientation and rotational interval:  $\Theta$ ,  $\Phi$ , and  $\beta$ . Angles  $\Theta$  and  $\Phi$  specify the position of the target relative to the direction of light propagation and, thus, specify the position of the target's internal axes within the lab frame.  $\beta$  specifies the rotation of the target about one of its internal

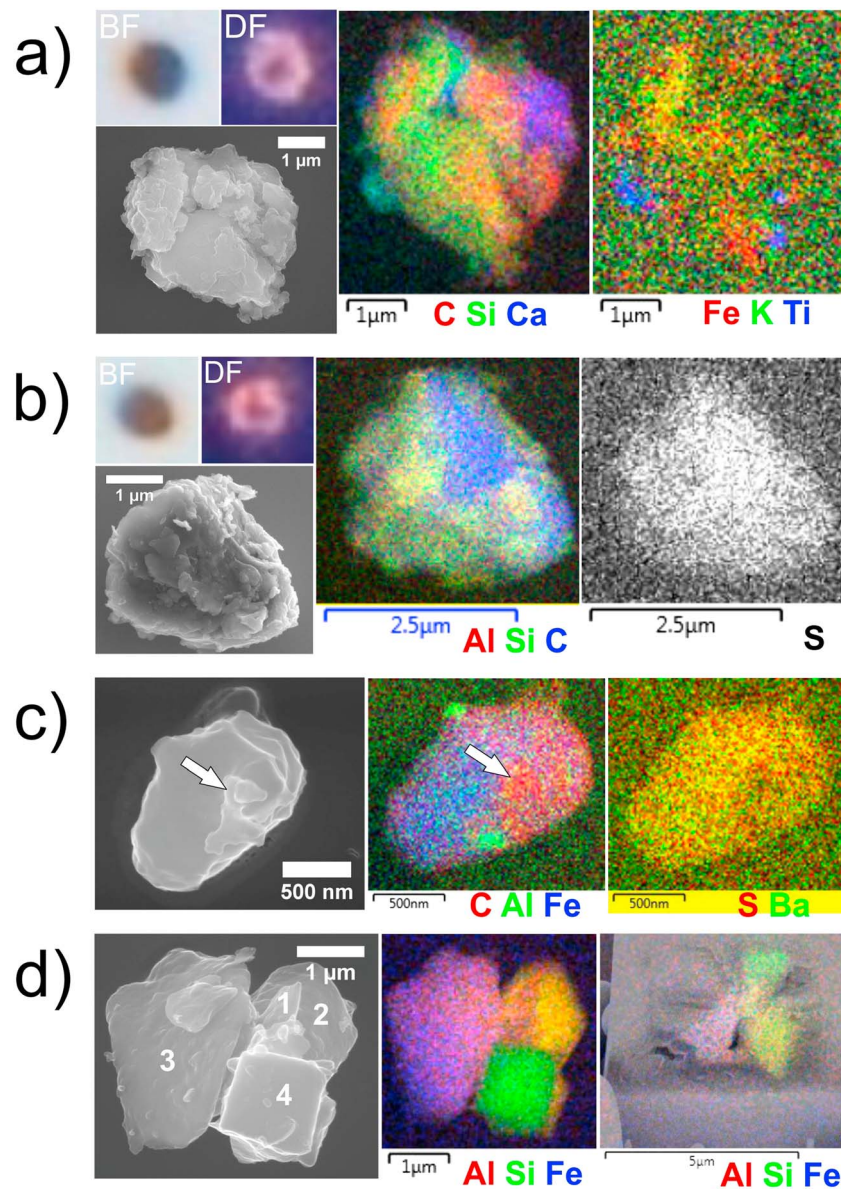


**Figure 1.** Microscopic images and high-resolution element maps for particles (a) LA1, (b) LA2, (c) LA3, and (d) LA4 from the Los Angeles sample. BF and DF indicate bright-field and dark-field light microscopy imaging; electron imaging is from secondary electrons. Arrows in Figure 1c indicate carbonaceous phase. See text for identities of phases 1–4 in Figure 1d.

axes. In this study,  $\Theta$  was positioned at angles corresponding to values 1, 0, and  $-1$  for  $\cos(\Theta)$ , i.e., at  $0^\circ$ ,  $90^\circ$ , and  $180^\circ$ .  $\Phi$  and  $\beta$  were incremented from  $0^\circ$  to  $360^\circ$  in steps of  $90^\circ$ . The incremental steps in  $\Theta$ ,  $\Phi$ , and  $\beta$  are a minimal number for this study to sufficiently represent particle rotation within the lab frame. Increasing the number of rotational steps would have resulted in an inordinate amount of time for DDSCAT to run the reference models for most particles due to the compositional complexity of the particles and the relatively large size parameters, which required targets to have a relatively large number of dipoles.

In addition to the rotation of the target, four scattering planes [Draine and Flatau, 2013] were used to intercept the calculated scattered light for determining the directions and intensities of light scattering. Two scattering planes aligned with the  $\hat{x}$ - $\hat{y}$  plane in the lab frame, and two scattering planes aligned with the  $\hat{x}$ - $\hat{z}$  plane. For each scattering plane, scattering was calculated at  $10^\circ$  intervals, from  $0^\circ$  to  $180^\circ$ , of the angle between the incident light beam and the scattered light beam. See the supporting information for additional information on algorithms used in DDSCAT. Error tolerance as set at  $10^{-3}$ .

**Table 1.** Elemental Noncarbon Composition<sup>a</sup> of Los Angeles Particles

Particle	Material Phase	Al (Al <sub>2</sub> O <sub>3</sub> ) <sup>b</sup>	Si (SiO <sub>2</sub> )	S (SO <sub>3</sub> )	K (K <sub>2</sub> O)	Ca (CaO)	Ti (TiO <sub>2</sub> )	Fe (FeO)	Ba (BaO)	
LA1	Element mass %	7.18	16.4	3.38	2.17	17.6	1.94	8.66		
	Oxide mass %	13.6	34.1	8.45	2.62	24.7	3.24	11.1		
LA2	Element mass %	12.4	18.9	7.75	1.66	1.54		9.89		
	Oxide mass %	23.4	40.4	19.4	2.01	2.16		12.7		
LA3	Element mass %	2.45	2.52	4.51		1.96		42.4	12.4	
	Oxide mass %	4.63	5.39	11.2		2.28		60.7	13.9	
LA4	Whole particle	Element mass %	9.44	30.8	0.25	1.02	0.51		10.7	
		Oxide mass %	17.8	65.8	0.63	1.23	0.71		13.8	
	Al silicate	Element mass %	12.0	34.4					2.82	
		Oxide mass %	22.7	73.7					3.63	
	Al silicate + Fe	Element mass %	11.7	22.4		1.62			22.1	
		Oxide mass %	22.2	47.9		1.95			28.5	
	Si containing	Element mass %	2.69	43.7					1.08	
		Oxide mass %	5.08	93.5					1.39	

<sup>a</sup>Oxygen is determined stoichiometrically but not shown in table as a separate element.

<sup>b</sup>Chemical compounds shown in parentheses are used by EDX analysis software to quantify composition. Compounds are not necessarily found in particles.

### 3. Results

#### 3.1. Phase Compositions and Volumes

##### 3.1.1. Carbon-Containing Particles (LA1 and LA2)

Figure 1 shows the microscopy and element maps for the particles selected from the LA sample. Two particles, LA1 and LA2, (Figures 1a and 1b) contained substantial amounts of inorganic carbon and mineral-like material. In these particles, quantification of carbon was not reliable because the samples were carbon coated to reduce charging by the electron beam. Two observations, however, support the presence of carbon. First, both LA particles appear black with bright-field light microscopy (BF in Figures 1a and 1b) and, thus, absorb light consistent with elemental carbon (EC). Second, the carbon *k*-ratio (mass concentration for sample divided by mass concentration for standard) from EDX for scanned areas of the particles was 6 to 7 times larger than the carbon *k*-ratio for equally sized areas of the wafer. For particles without carbon, *k*-ratios were only 2 to 3 times larger than the carbon *k*-ratio of the wafer. (Here enrichment of carbon with the particle may have been due to adventitious organic carbon on the particles' surface or a buildup of the deposited carbon coating within crevices on the particle surface.) Since the LA sampling site was near a major expressway, the particles are likely asphalt road wear. Asphalt concrete is commonly made by combining carbonaceous bitumen with ground rock [Thorpe and Harrison, 2008].

Table 1 shows the noncarbon element and oxide compositions of the particles. For LA1, FIB slicing revealed a network of mineral inclusions located toward the interior of the particle and occupying 58% of the particle volume based on FIB tomography. The rest of the particle volume consisted of carbon and sulfur as described below. (Particle phase volumes are shown in Table 3.) In the LA2 particle, carbon occupied a larger volume, 72%, while the mineral inclusion phase, located more toward the surface of the particle, constituted most of the remaining volume.

EDX element mapping of the elements provided insight into the identity of the inclusions. In LA1, the most abundant elements excluding carbon and oxygen were calcium (17.6 mass %) and silicon (16.4 mass %) followed by iron, aluminum, sulfur, potassium, and titanium (Table 1). The particle had distinctive calcium and titanium inclusions, assigned as calcite and rutile, occupying 10.0% and 1.59% of the particle volume, respectively (Table 3). The largest fraction of the inclusion volume involved silicates. Here the Al<sub>2</sub>O<sub>3</sub>/SiO<sub>2</sub> mass ratio (0.39) is identical with the clay mineral montmorillonite (0.39) [Anthony *et al.*, 2016]. However, the presence of iron and potassium suggested an additional silicate mineral. The K<sub>2</sub>O/FeO mass ratio (0.29), measured from the particle where the Fe X-ray signal was strongest, agrees reasonably well with that of biotite (0.46), given the particle's low abundance of potassium atoms (2.2 atomic %) and the higher probability of absorption of potassium *Kα* X-rays than iron *Kα* X-rays by silicon atoms. In addition, the Al<sub>2</sub>O<sub>3</sub>/SiO<sub>2</sub> mass ratio for biotite (0.38) is consistent with both the particle and montmorillonite. We assigned the larger silicate inclusion volume (74%) in LA1 to montmorillonite and the remaining silicate inclusions volume to biotite.

**Table 2.** Elemental Noncarbon Composition<sup>a</sup> of Seattle Particles

Particle	Material Phase	Na (Na <sub>2</sub> O) <sup>b</sup>	Al (Al <sub>2</sub> O <sub>3</sub> )	Si (SiO <sub>2</sub> )	S (SO <sub>3</sub> )	K (K <sub>2</sub> O)	Ca (CaO)	Mn (MnO)	Fe (Fe <sub>2</sub> O <sub>3</sub> )	Zn (ZnO)	
S1	Whole particle	Element Mass %	2.05	2.85	0.58	0.15	0.45	0.36	60.6	0.16	
		Oxide Mass %		3.88	6.09	1.46	0.18	0.63	0.47	86.6	0.20
	Fe matrix	Element Mass %		1.88	2.85	0.41	0.15	0.23	0.36	61.1	0.38
		Oxide Mass %		3.55	6.12	1.02	0.19	0.32	0.46	87.4	0.47
	Na containing	Element Mass %	14.2	1.89	2.62	0.05		0.14		49.3	0.14
		Oxide Mass %	19.2	3.56	5.61	0.11		0.19		70.5	0.17
	Ca and S containing	Element Mass %		0.96	1.69	6.70	0.39	6.61	0.14	46.5	0.80
		Oxide Mass %		1.82	3.62	16.73	0.47	9.24	0.19	66.53	1.00
S2	Whole particle	Element Mass %		9.26	29.2	0.71	1.71	1.62	9.80		
		Oxide Mass %		17.5	62.4	1.78	2.06	2.27	14.0		
	Na-Al silicate	Element Mass %		9.48	31.0	0.34	1.96	1.29	7.55		
		Oxide Mass %		17.8	66.3	0.86	2.36	1.80	10.8		
	Ca and S containing	Element Mass %		7.10	17.0	11.7	1.71	13.5			
		Oxide Mass %		13.4	36.5	29.2	2.06	18.9			
	Fe containing	Element Mass %		8.44	21.9				26.0		
		Oxide Mass %		15.9	46.9				37.2		
S3	Whole particle	Element Mass %		7.07	8.91	4.98	17.5		21.4		
		Oxide Mass %		13.4	19.1	12.4	24.5		30.7		
	Ca containing	Element Mass %					71.5				
		Oxide Mass %					100				
	Al-Ca silicate	Element Mass %		15.8	21.3	1.24	13.9		1.29		
		Oxide Mass %		29.9	45.6	3.10	19.5		1.85		
	Fe containing	Element Mass %		1.50	3.40	1.53	1.87		55.6		
		Oxide Mass %		2.84	7.27	3.83	2.61		79.5		
Ca and S containing	Element Mass %			3.80	19.8	30.4					
	Oxide Mass %			8.12	49.4	42.5					

<sup>a</sup>Oxygen is determined stoichiometrically but not shown in table as a separate element.

<sup>b</sup>Chemical compounds shown in parentheses are used by EDX analysis software to quantify composition. Compounds are not necessarily found in particles.

In the LA2 particle we assumed that the mineral inclusions observed with FIB tomography were silicates similar to those in LA1. The Al<sub>2</sub>O<sub>3</sub>/SiO<sub>2</sub> mass ratio was 0.58 (Table 1), substantially higher than for LA1. We approximated the Al<sub>2</sub>O<sub>3</sub>/SiO<sub>2</sub> ratio by including biotite (Al<sub>2</sub>O<sub>3</sub>/SiO<sub>2</sub> = 0.38) at a volume of 9.8% and the clay mineral kaolinite (Al<sub>2</sub>O<sub>3</sub>/SiO<sub>2</sub> = 0.86) at 6.8%.

In addition to carbon and mineral phases, sulfur was present in both particles. From the sulfur map for LA2 (Figure 1b), sulfur is homogeneously distributed, suggesting a sulfate layer, e.g., (NH<sub>4</sub>)<sub>2</sub>SO<sub>4</sub> as a pollutant secondary aerosol, occupying 5.3% of the particle volume (Table 3). Similarly, sulfur was observed in LA1, suggesting (NH<sub>4</sub>)<sub>2</sub>SO<sub>4</sub>, here occupying 10.7% of the particle volume.

### 3.1.2. Iron-Containing Particles (LA3 and S1)

In addition to the carbonaceous LA particles, iron particles from the LA and Seattle samples were selected. In particle LA3 (Figure 1c), iron was the most abundant element (42.4 mass %, Table 1) followed by barium (12.4 mass %) and <5 mass % of sulfur, silicon, aluminum, and calcium. Aluminum was detected from the FIB slices as individual surface and interior inclusions. In addition, a carbon adduct was detected (arrow in Figure 1c).

Light microscopy, which would have helped particle identification, was not obtainable for LA3. Instead, we relied on the iron oxidation state. While semiquantitative EDX analysis of light elements such as oxygen is problematic, it is still useful to compare the measured oxygen content with content assigned by stoichiometry. Here the measured oxygen content (35.4 mass %) was closer to the stoichiometric oxygen content for Fe<sup>+3</sup> hematite or goethite (32.4 mass %) than for Fe<sup>+2</sup> wustite (28.1 mass %). As either hematite or goethite, the iron oxide phase occupied 77% of the particle volume (Table 3). In addition, the element map (Figure 1c) shows sulfur distributed homogeneously, suggesting a surface layer of (NH<sub>4</sub>)<sub>2</sub>SO<sub>4</sub> as in LA1 and LA2. Based on the full elemental analysis, the remaining volume was assumed to be BaO (12 to 13%), (NH<sub>4</sub>)<sub>2</sub>SO<sub>4</sub> (7 to 8%), Al<sub>2</sub>O<sub>3</sub> (2%), and EC (soot) (2%). The presence of substantial barium with iron, and aluminum inclusions, suggests that the particle was an oxidized metal alloy, likely anthropogenic in origin.

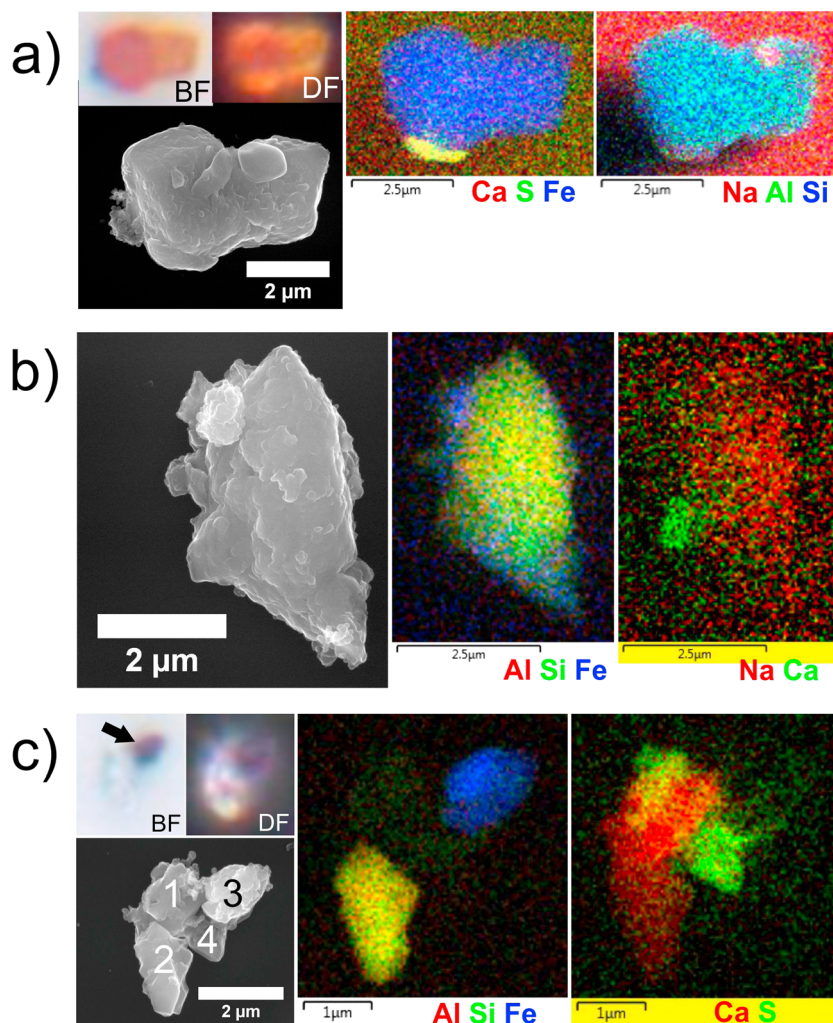


**Figure 2.** Microscopic images and high-resolution element maps for particles (a) S1, (b) S2, and (c) S3 from the Seattle sample. BF and DF indicate bright-field and dark-field light microscopy imaging; electron imaging is from secondary electrons. In Figure 2c, arrow indicates light-absorbing iron phase; see text for identities of phases 1–4.

For the iron-containing particle selected from the Seattle sample (S1), Table 2 shows the element and oxide compositions; Figure 2 shows the microscopy and element maps. Light microscopy images and element maps in Figure 2a indicate that the particle was nearly a pure iron oxide, with color of hematite or goethite. The calcium surface inclusion contained a comparable amount of sulfur and was identified as gypsum. The sodium phase was assumed to be a carbonate, as sodium hydrogen carbonate (mineral nahcolite). Two carbon phases are observed in the element maps and treated as EC. A minor amount of silicon was assumed to be an impurity. Phase volumes were determined from FIB tomography as follows: iron oxide 97%, sodium hydrogen carbonate 1.4%, gypsum 1%, and EC phases combined 1.1% (Table 4). In contrast to the iron-containing LA3 particle, purity of the iron phase, either hematite or goethite, and presence of mineral surface inclusions suggest that S1 was mineral in origin.

### 3.1.3. Aluminosilicate Mineral Particle (S2)

Seattle particle S2 (Figure 2b) most resembled a pure light-scattering silicate; however, minor phases affected its optical behavior. The main phase contained aluminum and sodium and, along with iron oxide, occupied 95.5% of the particle volume based on FIB tomography. The  $Al_2O_3/SiO_2$  mass ratio (Table 2) for the mineral phase (0.27) matches well the ratio for albite (0.30 [Anthony et al., 2016]). In addition, if we quantify sodium by deconvolving the interfering  $Ge\ L\alpha$  line, then the  $Na_2O/SiO_2$  mass ratio for the mineral phase is 0.13, which is reasonably close to the ratio for albite (0.17 [Anthony et al., 2016]). Surface inclusions containing calcium

and iron were also observed on the particle, occupying 3.4% and 1.1% of the volume, respectively. The inclusions were assigned, respectively, as gypsum based on the presence of sulfur and goethite.

While the iron inclusion was only 1.1% of the particle volume, iron was 9.2% of the particle's total mass. The inclusion itself contributed only about 5% of the particle's iron mass. The remaining iron was therefore associated with albite. If we assume that the albite-associated iron was an iron oxide impurity such as goethite, then the impurity occupied 9.3% of the albite volume based on density.

#### 3.1.4. Mineral Particles With Spatially Separated Phases (LA4 and S3)

In particles LA4 and S3 (Figures 1d and 2c), each phase was spatially distinct, resulting in particles that were morphologically complex. In both particles, four mineral phases were identified from EDX maps. In LA4, two aluminum silicate phases, labeled 1 and 2 in Figure 1d, had a  $\text{Al}_2\text{O}_3/\text{SiO}_2$  mass ratio (0.31, Table 1) that is nearly identical to albite (0.30) [Anthony *et al.*, 2016]. Albite contains substantial sodium (11 mass %) but little or no potassium and calcium. While potassium and calcium were not detected in the particle, sodium was detected but not quantified because of the overlap between the Na  $K\alpha$  and Ge  $L$  lines. The albite phases occupied the largest volume of the particle, 40%, based on FIB tomography.

Occupying 28% of the LA4 volume was an iron-containing silicate phase with 12% aluminum, 22% silicon, and 22% iron by mass (Table 1). Identity of the phase (labeled 3 in Figure 1d) is not certain, but a reasonable candidate is a solid solution of almandine and pyrope.  $\text{Al}_2\text{O}_3/\text{SiO}_2$  mass ratios in the particle ranged from 0.42 to 0.54. Almandine and pyrope have similar but slightly higher  $\text{Al}_2\text{O}_3/\text{SiO}_2$  mass ratios: 0.55 and 0.57, respectively [Anthony *et al.*, 2016]. For  $\text{FeO}/\text{SiO}_2$ , mass ratios from the particle ranged from 0.41 to 0.84. Iron is found in almandine ( $\text{FeO}/\text{SiO}_2$  0.97 to 1.2) but not pyrope. However, evidence for pyrope in the particle came from the detection of magnesium in a FIB slice. We used an average  $\text{FeO}/\text{SiO}_2$  of 0.75 for the particle, resulting in the iron silicate phase having 73% almandine and 27% pyrope by volume.

Alternatively, the iron silicate region of the particle may have been an iron oxide stratified with clay minerals such as illite and kaolinite.  $\text{Al}_2\text{O}_3/\text{SiO}_2$  mass ratios for illite and kaolinite vary widely (0.86 and 0.32, respectively [Anthony *et al.*, 2016]) and bracket the particle's ratio (0.42 to 0.54). For the iron oxide we consider hematite and goethite, which have different densities and thus different volumes. For the phase consisting of illite and kaolinite with hematite, volumes were 21.5%, 8.04%, and 7.9%, respectively (Table 3). With goethite, volumes were 19.7%, 7.36%, and 10.4%, respectively. The remaining phase in LA4 (Si containing, labeled 4 in Figure 1d) was quartz (94 mass %  $\text{SiO}_2$ , Table 1), occupying 22% of the particle volume.

As in LA4 particle, the Seattle S3 particle (Figure 2c) had four distinct mineral phases. The largest phase (labeled 1 in Figure 2c), containing calcium (71 mass %, Table 2) but with no detected anion, was assumed to be the carbonate calcite at 31.3% of the particle volume (Table 4). A silicate phase (labeled 2), 26.3% of the particle volume, had a  $\text{CaO}/\text{SiO}_2$  mass ratio of 0.43 and a  $\text{Al}_2\text{O}_3/\text{SiO}_2$  mass ratio of 0.66, which is consistent with anorthite whose respective ratios are 0.42 and 0.77 [Anthony *et al.*, 2016].  $\text{Al}_2\text{O}_3/\text{SiO}_2$  from the particle is lower than that of anorthite due likely to the presence of albite, which commonly exists in solution with anorthite. The next largest phase, at 21.9% of the volume (labeled 3), contained 55.6 mass % iron and much smaller amounts (<5 mass %) of aluminum, silicon, and sodium. Light microscopy (Figure 2c) shows a black absorbing phase (arrow). It is assigned here as wustite, FeO. The smallest phase (labeled 4), at 20.5% of the volume, largely contained only calcium (30.4 mass %) and sulfur (19.8 mass %), consistent with gypsum.

#### 3.2. Optical Property Modeling

For each particle, the reference model included the overall particle size and shape, void spaces if any, and the structure of each identified material phase derived from SEM-EDX and FIB tomography, as discussed previously. The reference models were assumed to be the most accurate representations of the shape and heterogeneity of the selected particles. Figure 3 shows the 3-D representations of the particles. Optical properties from two types of test models were then compared to the reference models:

1. *Homogeneous spatial models* included particle size, actual shape, and void spaces but treated the particle's material phases as a single phase by combining the complex refractive indexes. These models represented the actual spatial configuration of the particle, but without individual phases resolved by composition, i.e., as a homogeneous particle.
2. *Geometric models* approximated the particle's size, shape, and composition with spheres, cubes, and tetrahedra. To represent a particle's composition heterogeneity, the particle was modeled as a collection of

**Table 3.** Assignment of Complex Refractive Indexes to Particle Phases: Los Angeles Particles

Particle	Material Phase	Percent Volume	Complex Refractive Index		References			
			Real Part	Imaginary Part				
LA1	Single phases	BC	36.8	1.95	0.79	<i>Bond and Bergstrom</i> [2006]		
		Graphite	36.8	2.65	1.39	<i>Stagg and Charalampopoulos</i> [1993]		
		Montmorillonite	42.9	1.52	0.000035	<i>Anthony et al.</i> [2016] and <i>Egan and Hilgeman</i> [1979, Table V-19]		
	Combined phases <sup>a</sup>	Calcite	10.0	1.49	~0	<i>Anthony et al.</i> [2016]		
		(NH <sub>4</sub> ) <sub>2</sub> SO <sub>4</sub>	5.30	1.53	~0	<i>Toon et al.</i> [1976]		
		Biotite	3.39	1.65	0.00034	<i>Anthony et al.</i> [2016] and <i>Egan and Hilgeman</i> [1979, Table V-22]		
		Rutile	1.59	2.90	~0	<i>Anthony et al.</i> [2016]		
		BC + (NH <sub>4</sub> ) <sub>2</sub> SO <sub>4</sub> + Montmorillonite	100	1.746	0.389	<i>Bond and Bergstrom</i> [2006], <i>Toon et al.</i> [1976], <i>Anthony et al.</i> [2016], and <i>Egan and Hilgeman</i> [1979, Tables V-19 and V-22]		
		+ Calcite + Biotite + Rutile						
		Graphite + (NH <sub>4</sub> ) <sub>2</sub> SO <sub>4</sub> + Montmorillonite + Calcite + Biotite + Rutile	100	2.071	0.725	<i>Stagg and Charalampopoulos</i> [1993], <i>Toon et al.</i> [1976], <i>Anthony et al.</i> [2016], and <i>Egan and Hilgeman</i> [1979, Tables V-19 and V-22]		
LA2	Single phases	BC (soot)	72.5	1.95	0.79	<i>Bond and Bergstrom</i> [2006]		
		Graphite	72.5	2.65	1.39	<i>Stagg and Charalampopoulos</i> [1993]		
		(NH <sub>4</sub> ) <sub>2</sub> SO <sub>4</sub>	10.7	1.53	~0	<i>Toon et al.</i> [1976]		
		Biotite	9.78	1.65	0.00034	<i>Anthony et al.</i> [2016] and <i>Egan and Hilgeman</i> [1979, Table V-22]		
		Kaolinite	6.78	1.56	0.000038	<i>Anthony et al.</i> [2016] and <i>Egan and Hilgeman</i> [1979, Table V-15]		
	Combined phases <sup>a</sup>	BC + (NH <sub>4</sub> ) <sub>2</sub> SO <sub>4</sub> + Biotite + Kaolinite	99.8	1.807	0.479	<i>Bond and Bergstrom</i> [2006], <i>Toon et al.</i> [1976], <i>Anthony et al.</i> [2016], and <i>Egan and Hilgeman</i> [1979, Tables V-22 and V-15]		
		Graphite + (NH <sub>4</sub> ) <sub>2</sub> SO <sub>4</sub> + Biotite + Kaolinite	99.8	2.215	0.874	<i>Stagg and Charalampopoulos</i> [1993], <i>Toon et al.</i> [1976], <i>Anthony et al.</i> [2016], and <i>Egan and Hilgeman</i> [1979, Tables V-22 and V-15]		
		LA3	Single phases	Hematite	76.9	2.91	0.1	<i>Anthony et al.</i> [2016] and <i>Sokolik and Toon</i> [1999]
				Limonite	76.7	2.46	0.0042	<i>Anthony et al.</i> [2016] and <i>Egan and Hilgeman</i> [1979, Table V-16]
				Goethite	76.7	2.46	0.08	<i>Anthony et al.</i> [2016] and <i>Bedidi and Cervelle</i> [1993]
Combined phases <sup>a</sup>	BaO		11.8 <sup>b</sup> 13.3 <sup>c</sup>	1.99	0.0003	<i>Anderson and Hensley</i> [1975]		
	(NH <sub>4</sub> ) <sub>2</sub> SO <sub>4</sub>		8.44 <sup>b</sup> 7.11 <sup>c</sup>	1.53	~0	<i>Toon et al.</i> [1976]		
	Al <sub>2</sub> O <sub>3</sub>	1.83	1.76	~0	<i>Anthony et al.</i> [2016]			
	BC	0.66	1.95	0.79	<i>Bond and Bergstrom</i> [2006]			
	Hematite + BaO + (NH <sub>4</sub> ) <sub>2</sub> SO <sub>4</sub> + Al <sub>2</sub> O <sub>3</sub>	98.9	2.566	0.0721	<i>Anthony et al.</i> [2016], <i>Sokolik and Toon</i> [1999], <i>Anderson and Hensley</i> [1975], and <i>Toon et al.</i> [1976]			
Combined phases <sup>a</sup>	Limonite + BaO + (NH <sub>4</sub> ) <sub>2</sub> SO <sub>4</sub> + Al <sub>2</sub> O <sub>3</sub>	98.9	2.293	0.00316	<i>Anthony et al.</i> [2016], <i>Egan and Hilgeman</i> [1979, Table V-16], <i>Anderson and Hensley</i> [1975], and <i>Toon et al.</i> [1976]			
	Goethite + BaO + (NH <sub>4</sub> ) <sub>2</sub> SO <sub>4</sub> + Al <sub>2</sub> O <sub>3</sub>	98.9	2.293	0.0600	<i>Anthony et al.</i> [2016], <i>Bedidi and Cervelle</i> [1993], and <i>Anderson and Hensley</i> [1975]			
	LA4	Single phases	Albite <sup>d</sup>	1.32 38.9	1.54	0.000035	<i>Anthony et al.</i> [2016] and <i>Egan and Hilgeman</i> [1979, Table V-10]	
Quartz			22.2	1.55	~0	<i>Anthony et al.</i> [2016]		
Almandine			27.4	1.83	0.00034	<i>Anthony et al.</i> [2016] and <i>Egan and Hilgeman</i> [1979, Table V-22]		
Pyrope			10.1	1.71	0.00034	<i>Anthony et al.</i> [2016] and <i>Egan and Hilgeman</i> [1979, Table V-22]		
Illite			21.5 <sup>e</sup> 19.7 <sup>f</sup>	1.41	0.00071	<i>Anthony et al.</i> [2016] and <i>Egan and Hilgeman</i> [1979, Table V-14]		
Kaolinite			8.04 <sup>e</sup> 7.36 <sup>f</sup>	1.56	0.000038	<i>Anthony et al.</i> [2016] and <i>Egan and Hilgeman</i> [1979, Table V-15]		
Hematite			7.91	2.91	0.1	<i>Anthony et al.</i> [2016] and <i>Sokolik and Toon</i> [1999]		

**Table 3.** (continued)

Particle	Material Phase	Percent Volume	Complex Refractive Index		References
			Real Part	Imaginary Part	
	Limonite	10.4	2.46	0.0042	<i>Anthony et al. [2016] and Egan and Hilgeman [1979, Table V-16]</i>
	Goethite	10.4	2.46	0.08	<i>Anthony et al. [2016] and Bedidi and Cervelle [1993]</i>
Combined phases <sup>a</sup>	Albite + Almandine + Pyrope + Quartz + Albite	99.9	1.637	0.000136	<i>Anthony et al. [2016] and Egan and Hilgeman [1979, Tables V-10 and V-22]</i>
	Albite + Illiite/Kaolinite/Hematite + Quartz + Albite	99.9	1.598	0.00433	<i>Anthony et al. [2016], Egan and Hilgeman [1979, Tables V-10, V-14, and V-15], and Sokolik and Toon [1999]</i>
	Albite + Illiite/Kaolinite/Limonite + Quartz + Albite	99.9	1.598	0.000471	<i>Anthony et al. [2016] and Egan and Hilgeman [1979, Tables V-10, V-14, V-15, and V-16]</i>
	Albite + Illiite/Kaolinite/Goethite + Quartz + Albite	99.9	1.598	0.00580	<i>Anthony et al. [2016], Egan and Hilgeman [1979, Tables V-10, V-14, and V-15], and Bedidi and Cervelle [1993]</i>

<sup>a</sup>Optical properties for combined phases are calculated from Maxwell-Garnett dielectric function (see equations (1)–(3)). The real part of the Maxwell-Garnett function  $\epsilon' = n^2 - k^2$ , where  $n$  and  $k$  are the real and imaginary parts of the refractive index. Likewise, the imaginary part of the Maxwell-Garnett function  $\epsilon'' = 2nk$ .

<sup>b</sup>Volume if phase is associated with hematite.

<sup>c</sup>Volume if phase is associated with goethite.

<sup>d</sup>Particle contains two albite phases.

<sup>e</sup>Volume if phase is associated with hematite.

<sup>f</sup>Volume if phase is associated with either goethite or limonite.

spheres, each sphere corresponding to a separate phase or group of the phases (*heterogeneous geometric models*). In addition, particles were modeled with a homogeneous composition as a single sphere, cube, and tetrahedron (*homogeneous geometric models*).

As mentioned previously, we generated different model treatments for each particle by using different compositions of the absorbing phase. Along with the percent volume of each phase, Tables 3 and 4 show the various material phases used for each particle and the complex refractive index used for each phase. The tables also show how phases were combined within a particle to represent composition homogeneity, the percent volume for a combined phase, and the complex refractive index for the combined phase. A homogeneous composition was applied to the whole particle as for the homogeneous spatial model described above. Or it was applied to a particular inclusion phase observed with FIB tomography but which appeared to consist of two mineral minerals that could not be resolved with FIB tomography. An example is illite and kaolinite in particle LA4.

For determining its refractive index, a combined phase was treated as an inclusion within a matrix using the Maxwell-Garnett dielectric function [Bohren and Wickramasinghe, 1977]. Maxwell-Garnett is one of the many effective medium approximations for determining the average complex refractive index of a multiphase particle, including the Bruggeman approximation and other size-versatile extended effective medium approximations, whereby the inclusion diameter is assumed to be smaller than the incident wavelength [Chylek et al., 2000]. In combining two phases with Maxwell-Garnett, the inclusion is assumed to be the smaller phase embedded in a larger matrix phase [Bohren and Huffman, 1983]:

$$\epsilon_{av} = \epsilon_m \left[ 1 + \frac{3f \left( \frac{\epsilon_{in} - \epsilon_m}{\epsilon_m + 2\epsilon_m} \right)}{1 - f \left( \frac{\epsilon_{in} - \epsilon_m}{\epsilon_{in} + 2\epsilon_m} \right)} \right] \quad (1)$$

Here  $\epsilon_{av}$  is the average dielectric function for the combined phase,  $f$  is the volume fraction of the inclusion,  $\epsilon_{in}$  is the dielectric function for the inclusion, and  $\epsilon_m$  is the dielectric function for the matrix, whereby the dielectric function is a complex number consisting of the real part  $\epsilon'_{av,in,m}$  and the imaginary part  $\epsilon''_{av,in,m}$ .  $\epsilon_{av}$  is necessarily an approximation because theoretical treatment of the Maxwell-Garnett function assumes that the inclusions are spherical [Bohren and Wickramasinghe, 1977].

**Table 4.** Assignment of Complex Refractive Indexes to Particle Phases: Seattle Particles

Particle	Material Phase	Percent Volume	Complex Refractive		References		
			Index Real Part	Imaginary Part			
S1	Single phases	Goethite	96.6	2.46	0.09	<i>Anthony et al.</i> [2016] and <i>Bedidi and Cervelle</i> [1993]	
		Limonite	96.6	2.46	0.0042	<i>Anthony et al.</i> [2016] and <i>Egan and Hilgeman</i> [1979, Table V-16]	
		Sodium hydrogen carbonate (Nahcolite)	1.36	1.58	~0	<i>Anthony et al.</i> [2016]	
		Gypsum	1.00	1.53	~0	<i>Anthony et al.</i> [2016]	
		Soot	0.66	1.95	0.79	<i>Bond and Bergstrom</i> [2006]	
		Graphite	0.43	2.65	1.39	<i>Stagg and Charalampopoulos</i> [1993]	
		Albite	95.5	1.57	0.000035	<i>Anthony et al.</i> [2016] and <i>Egan and Hilgeman</i> [1979, Table V-10]	
S2	Single phases	Gypsum	3.42	1.53	~0	<i>Anthony et al.</i> [2016]	
		Goethite	1.12	2.46	0.09	<i>Anthony et al.</i> [2016] and <i>Bedidi and Cervelle</i> [1993]	
		Wustite	1.12	2.42	0.64	<i>Henning et al.</i> , 1995	
	Combined phases <sup>a</sup>	Albite + Gypsum + Goethite	100	1.547	0.000734	<i>Anthony et al.</i> [2016], <i>Egan and Hilgeman</i> [1979, Table V-10], and <i>Bedidi and Cervelle</i> [1993]	
		Albite + Goethite + Gypsum + Goethite(inclusion)	100	1.618	0.00643	<i>Bedidi and Cervelle</i> [1993]	
		Albite + Gypsum + Wustite	100	1.547	0.00506	<i>Anthony et al.</i> [2016], <i>Egan and Hilgeman</i> [1979, Table V-10], and <i>Henning et al.</i> [1995]	
		Albite + Wustite + Gypsum + Wustite(inclusions)	100	1.607	0.0378	<i>Hilgeman</i> [1979, Table V-10], and <i>Henning et al.</i> [1995]	
	S3	Single phases	Calcite	31.3	1.49	~0	<i>Anthony et al.</i> [2016]
			Anorthite	26.3	1.59	0.000035	<i>Anthony et al.</i> [2016] and <i>Egan and Hilgeman</i> [1979, Table V-10]
			Wustite	21.9	2.42	0.64	<i>Henning et al.</i> [1995]
Goethite			21.9	2.46	0.09	<i>Anthony et al.</i> [2016] and <i>Bedidi and Cervelle</i> [1993]	
Limonite			21.9	2.46	0.0042	<i>Anthony et al.</i> [2016] and <i>Egan and Hilgeman</i> [1979, Table V-16]	
Gypsum			20.5	1.53	~0	<i>Anthony et al.</i> [2016]	
Combined phases <sup>a</sup>			Calcite + Anorthite + Wustite + Gypsum	100	1.731	0.112	<i>Anthony et al.</i> [2016], <i>Egan and Hilgeman</i> [1979, Table V-10], and <i>Henning et al.</i> [1995]
	Calcite + Anorthite + Goethite + Gypsum	100	1.722	0.0156	<i>Anthony et al.</i> [2016], <i>Egan and Hilgeman</i> [1979, Table V-10], and <i>Bedidi and Cervelle</i> [1993]		
	Calcite + Anorthite + Limonite + Gypsum	100	1.722	0.000731	<i>Anthony et al.</i> [2016] and <i>Egan and Hilgeman</i> [1979, Tables V-10 and V-16]		

<sup>a</sup>Optical properties for combined phases are calculated from Maxwell-Garnett dielectric function (see equations (1)–(3)). The real part of the Maxwell-Garnett function  $\epsilon' = n^2 - k^2$ , where  $n$  and  $k$  are the real and imaginary parts of the refractive index. Likewise, the imaginary part of the Maxwell-Garnett function  $\epsilon'' = 2nk$ .

The complex dielectric function for the combined phase is related to the real part of the complex refractive index ( $n_{av}$ ) and the imaginary part of the complex refractive index ( $k_{av}$ ) as follows [Bohren and Huffman, 1983]:

$$n_{av} = \left[ \frac{\sqrt{\epsilon_{av}'^2 + \epsilon_{av}''^2} + \epsilon_{av}'}{2} \right]^{1/2} \quad (2)$$

$$k_{av} = \left[ \frac{\sqrt{\epsilon_{av}'^2 + \epsilon_{av}''^2} - \epsilon_{av}'}{2} \right]^{1/2} \quad (3)$$

When combining three or more phases with different complex refractive indexes to produce a homogeneous particle, the average complex dielectric function was generated via equation (1) by sequentially combining phases such that the average dielectric function from the first two phases now became the matrix for combining the third phase, which was then the inclusion, etc. For example, in the LA3 particle, hematite as the matrix phase was combined with BaO as the inclusion phase in proportions by volume of 0.88 and

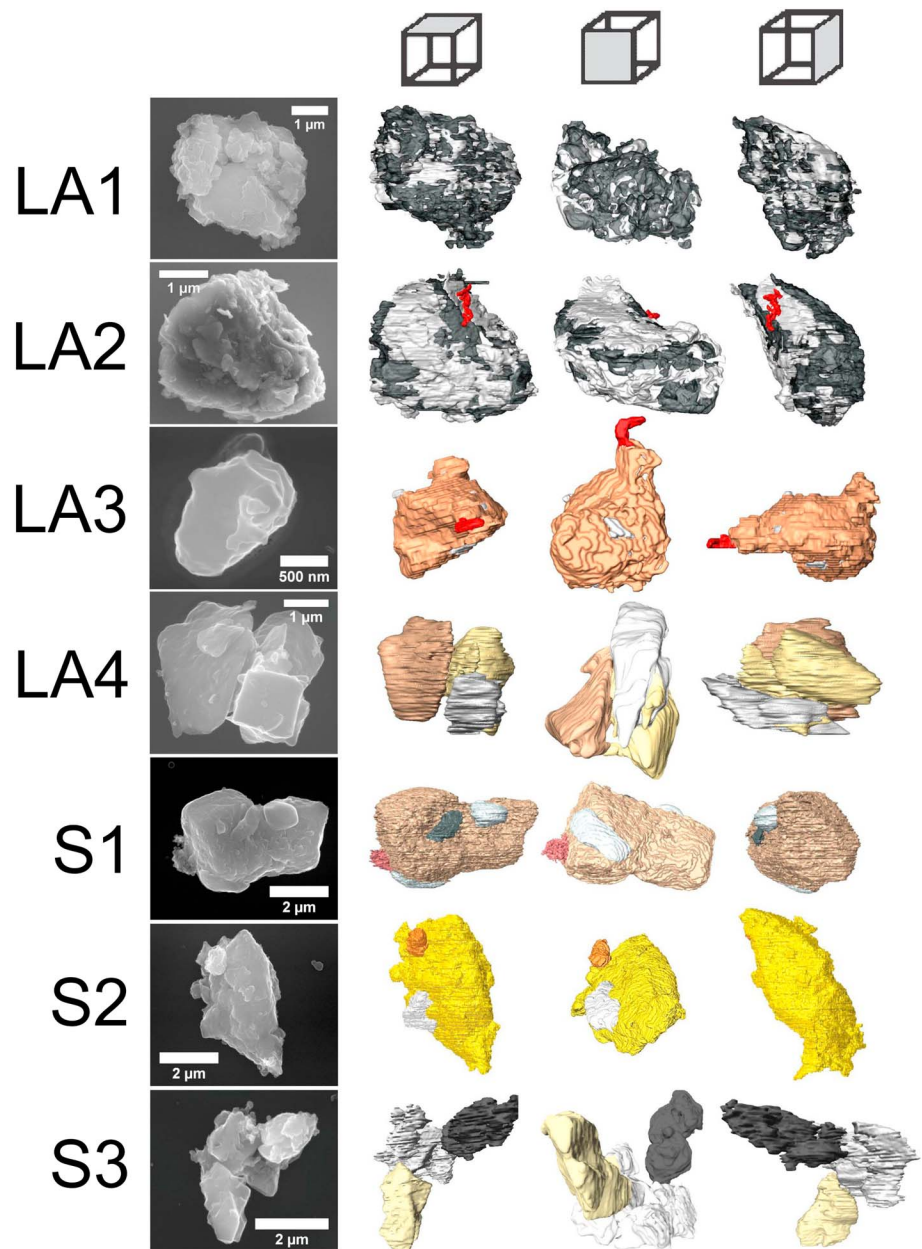


**Figure 3.** *x-z*, *x-y*, and *y-z* views of three-dimensional spatial models of particles (and associated secondary electron images) for Los Angeles particles LA1–LA4 and Seattle particles S1–S3.

0.12, respectively, which corresponded to their relative volumes in the particle. The average complex refractive index for the combination was  $2.796 + 0.0879i$ . Next, the hematite/BaO matrix was combined with  $(\text{NH}_4)_2\text{SO}_4$  as the inclusion phase in proportions of 0.91 and 0.09. Then the hematite/BaO/ $(\text{NH}_4)_2\text{SO}_4$  matrix was combined with  $\text{Al}_2\text{O}_3$  as the inclusion in proportions of 0.95 and 0.05. The resulting complex refractive index was  $2.566 + 0.072i$ .

An important criterion with DDA is that the number of dipoles should be sufficient such that  $|m|kd < 1$ . Here  $|m|$  is the magnitude of the complex refractive index,  $k = 2\pi/\lambda$  ( $\lambda = 0.589 \mu\text{m}$ ), and  $d$  is the interdipole distance [Draine and Flatau, 1994]. If the number of dipoles is large enough so that  $d$  is small relative to the particle size, then DDA is suitable when the size parameter  $x = ka_{\text{eff}} \leq 25$  (where  $a_{\text{eff}}$  is the radius of the particle as a sphere with the same volume) and  $m$  is moderately sized, i.e.,  $|m - 1| \leq 2$  [Draine and Flatau, 2013]. In this study,  $|m|kd < 1$  was satisfied by all particles as shown in Table 5.

**Table 5.** Particle Sizes, Size Parameters ( $x$ ), Refractive Index Magnitudes ( $|m|$ ), and Interdipole Distances ( $d$ ) for Meeting the DDA Criterion  $|m|kd < 1$ 

Particle	Phase Treatment	Diameter <sup>a</sup>	$x$	$ m $	$d$	$ m kd$
LA1	BC	2.53	13.5	1.789	0.0422	0.805
	graphite			2.194		0.987
LA2	BC	2.09	11.2	1.869	0.0375	0.748
	graphite			2.381		0.953
LA3	hematite	1.28	6.85	2.567	0.0292	0.799
	limonite			2.293		0.714
	goethite			2.294		0.714
LA4	silicate	2.83	15.1	1.637	0.0505	0.882
	hematite			1.598		0.861
	limonite			1.598		0.861
	goethite			1.598		0.861
S1	goethite	3.37	18.0	2.459	0.0312	0.819
	limonite			2.460		0.820
S2	goethite	2.72	14.5	1.618	0.0270	0.465
	wustite			1.607		0.465
S3	wustite	2.05	10.9	1.735	0.359	0.663
	goethite			1.722		0.659
	limonite			1.722		0.659

<sup>a</sup>Diameter ( $\mu\text{m}$ ) of the particle as a sphere with the same volume.

Particle optical properties were calculated as extinction ( $Q_{\text{ext}}$ ) and scattering ( $Q_{\text{sca}}$ ) efficiencies and the asymmetry parameter ( $\langle \cos \theta \rangle$ ) along with SSA. Efficiencies are the optical cross sections normalized by the cross-sectional area of a sphere with the same volume as the particle [Draine and Flatau, 2013]. Efficiencies and  $\langle \cos \theta \rangle$  are calculated at each orientation of the particle within the computational lab frame and then reported as the average for all orientations. The absorption efficiency ( $Q_{\text{abs}}$ ) was determined as the difference between the extinction and scattering efficiencies. Tables S1 to S7 in the supporting information show the optical efficiencies,  $\langle \cos \theta \rangle$ , and SSA for the reference models, homogeneous spatial models, and geometric models of the various composition treatments for each particle.

### 3.2.1. Carbon-Containing Particles (LA1 and LA2)

In particles LA1 and LA2 we consider EC as graphite or black carbon from incomplete combustion, i.e., soot-like carbon. As mentioned previously, FIB tomography revealed that the carbon phase was toward the periphery of LA1, but toward the interior of LA2. For the geometric models of LA1 and LA2 exhibiting heterogeneity, we employed spherical core-shell configurations: mineral phases as the core and EC as the shell for LA1 (symbolically as filled black circle); EC as the core and the mineral phases as the shell for LA2 (symbolically as filled black circle). In each case, the  $(\text{NH}_4)_2\text{SO}_4$  phase was assumed to be peripheral; thus,  $(\text{NH}_4)_2\text{SO}_4$  was combined with EC for the shell in LA1 and with the mineral phases for the shell in LA2. We focus on how the core-shell models compared with the homogeneous geometric models relative to the reference models.

LA1 and LA2 can be generalized as highly absorbing heterogeneous particles with some surface texture and aspect ratios close to 1. Figure 4 compares the  $Q_{\text{ext}}$ , SSA, and  $\langle \cos \theta \rangle$  for the various models. In general, variation in optical properties for reference models between the two particles, whether with BC or graphite, is overshadowed in each case by differences between test models and the respective reference model. For  $Q_{\text{ext}}$ , reference models for the two particles average 3.00. Among the test models,  $Q_{\text{ext}}$  (Figure 4a) for tetrahedral models come closest to the respective reference models, averaging 3.06 for the two particles.  $Q_{\text{ext}}$  for the spherical models of the two particles are well below values for the respective reference models:  $Q_{\text{ext}}$  for the single-sphere models of the two particles average 2.40, while  $Q_{\text{ext}}$  for the core-shell models average 2.37.

For SSA (Figure 4b), the homogeneous spatial models, whether with graphite or BC, come closest to the respective reference models, within 4%. In contrast, SSA from the core-shell model for LA1 is as much as 12% above the reference model (graphite case), while the core-shell model for LA2 is as much as 10% below the reference model. For the most part, homogeneous geometric models (sphere, cube, and tetrahedron) are

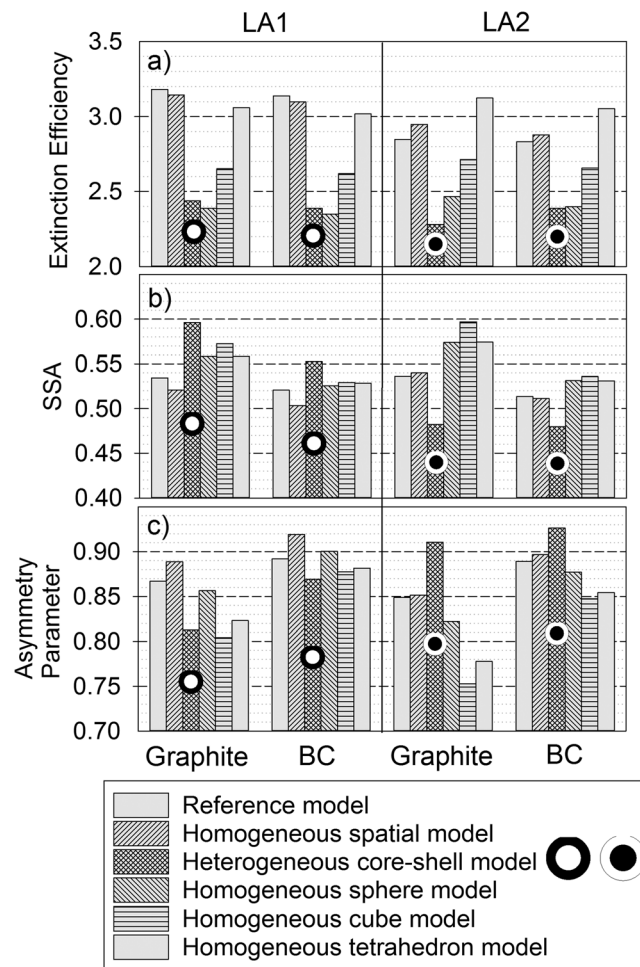


**Figure 4.** Optical properties (a)  $Q_{ext}$ , (b) SSA, and (c)  $\langle \cos \theta \rangle$  for carbon-containing particles LA1 and LA2 with either graphite or BC as the carbonaceous phase. The incident wavelength is 589 nm. Reference models and homogeneous spatial models are based on FIB tomography. Geometric models (core-shell, homogeneous sphere, cube, and tetrahedron) are based on particle size and composition information from FIB tomography and element mapping. The core-shell model with mineral core and EC shell is shown symbolically as empty black circle; the model with EC core and mineral shell is shown symbolically as filled black circle.

well. Particle S1 was shaped like a rectangular cuboid and had three small but prominent surface inclusions, two of which (gypsum and  $\text{NaHCO}_3$ ) were strongly light scattering.

Figure 5 compares  $Q_{ext}$ , SSA, and  $\langle \cos \theta \rangle$  from models for the different iron oxide compositions in LA3 and S1. Reference models for both particles show that SSA and  $\langle \cos \theta \rangle$  change substantially with the iron oxide composition, while  $Q_{ext}$  does not. For LA3, closest on average to the reference models for  $Q_{ext}$  (Figure 5a) are the tetrahedron and homogeneous spatial models. The spherical and cubic homogeneous models and the two-sphere heterogeneous model exhibit variation in  $Q_{ext}$  with the iron oxide composition that does not exist in the reference models; thus, these models appear to be problematic. For particle S1, only the homogeneous spatial model appears to adequately approximate  $Q_{ext}$  for both iron oxides (Figure 5b).

The principal factor affecting SSA for both particles is the identity (more precisely the refractive index) of the iron oxide. From the reference models, SSA levels for LA3 (Figure 5c) with hematite and goethite are low yet similar, 0.56 and 0.57, respectively, likewise, for particle S1 with goethite (0.55, Figure 5d). Generally, SSAs

closer to the reference models than the core-shell models. Thus, the core-shell models were less successful than the homogeneous geometric models for approximating extinction and SSA and, therefore, failed to account for composition heterogeneity.

For the asymmetry parameter (Figure 4c), a trend exists among all models in that  $\langle \cos \theta \rangle$  is larger with particles containing BC than with graphite. Nevertheless, core-shell models underestimate  $\langle \cos \theta \rangle$  for LA1, but overestimate it for LA2, behavior that is the reverse of that for SSA and that other test models do not exhibit.

### 3.2.2. Iron-Containing Particles (LA3 and S1)

Like particles LA1 and LA2, particles LA3 and S1 were largely light absorbing, but in this case due to iron oxide. LA3 was 77% iron oxide by volume, and S1 was nearly all iron oxide (97%) based on FIB tomography. We modeled the iron oxide phase as hematite, goethite, or limonite. As a variation of goethite,  $\text{FeO}(\text{OH})$ , limonite has smaller imaginary part of the complex refractive indexes at 600 nm (Table 3) as reported by Egan and Hilgeman [Egan and Hilgeman, 1979].

In addition to the  $\text{BaO}$ ,  $\text{Al}_2\text{O}_3$ , and  $(\text{NH}_4)_2\text{SO}_4$  phases associated with the iron oxide, LA3 had a small but prominent EC (soot-like) adduct (arrow in Figure 1c). To account for this adduct, we used a two-sphere heterogeneous geometric model. As with other particles, we employed the homogeneous spatial and geometric test models as

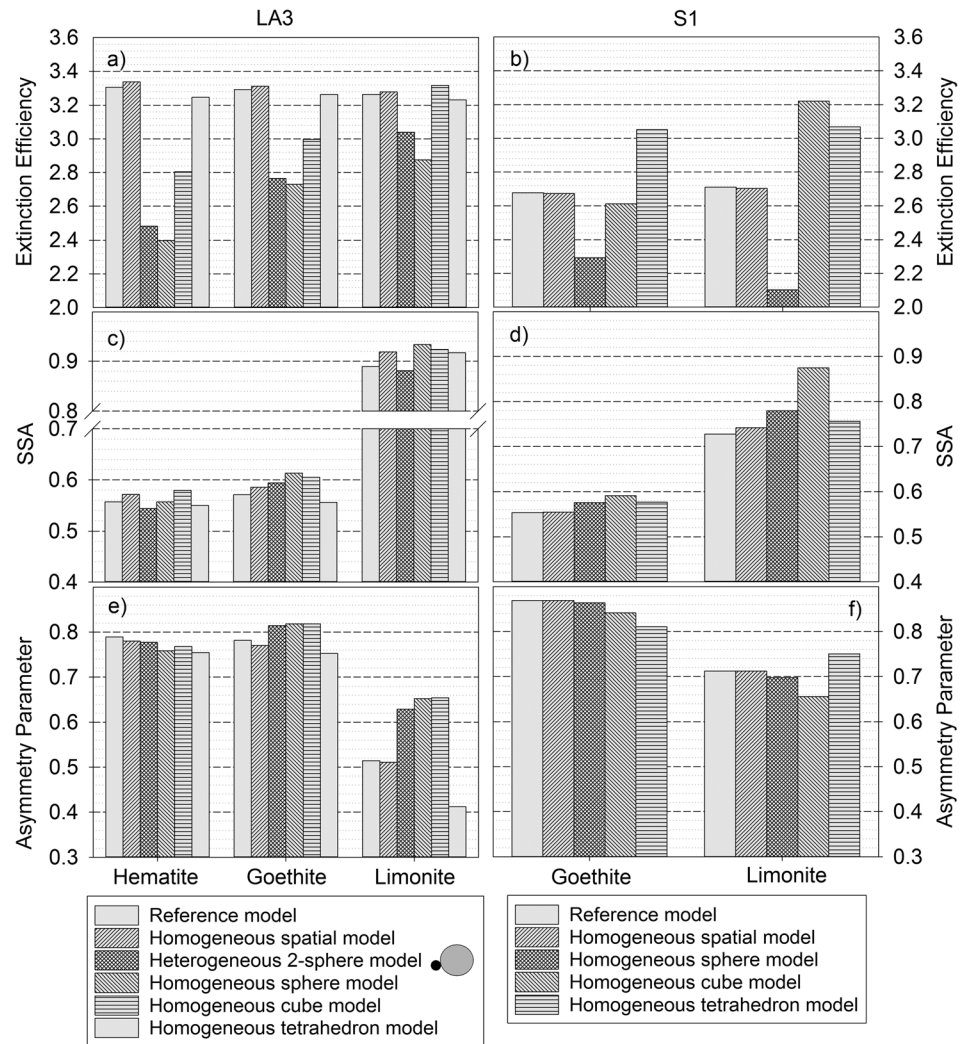


**Figure 5.** Optical properties (a, b)  $Q_{ext}$  (c, d) SSA, and (e, f)  $\langle \cos \theta \rangle$  for iron-containing particles LA3 and S1 with either hematite, goethite, or limonite as the iron-containing phase. Incident wavelength is 589 nm.

from the test models are remarkably close to the respective reference models, with the possible exception of the cubic model SSA for particle S1 with limonite. This case, in which SSA is 20% higher than the reference model, is perhaps surprising because S1 appears to have dihedral angles that are close to cuboidal (Figure 2a). Nevertheless, for the most part test models are sufficient to account for SSA variation due to the presence of iron oxides with varying refractive indexes.

The asymmetry parameter (Figures 5e and 5f) is also affected largely by the identity of the iron oxide, as indicated by all models for both particles LA3 and S1. Particles with higher absorbing hematite and goethite phases have similar but larger  $\langle \cos \theta \rangle$  values than with lower absorbing limonite. Thus, test models generally exhibit differences in scattering directionality due to different iron oxide compositions. Nevertheless, greater disparity in  $\langle \cos \theta \rangle$  among test models exists for particle LA3 (Figure 5e) than S1, particularly with limonite. For example, the heterogeneous two-sphere model for LA3 is much closer to the reference model for hematite and goethite than for limonite.

### 3.2.3. Aluminosilicate Mineral Particle (S2)

Particle S2 largely contained the aluminosilicate albite (87 to 88% by volume, Table 4) and smaller amounts of iron oxide, modeled as light-absorbing goethite or wustite. As such, S2 provided a contrast with particles LA3 and S1, which had inversely large amounts of light-absorbing iron oxide. For  $Q_{ext}$  (Figure 6a), the tetrahedral model and homogeneous spatial models with either iron oxide phase are closest to the respective reference

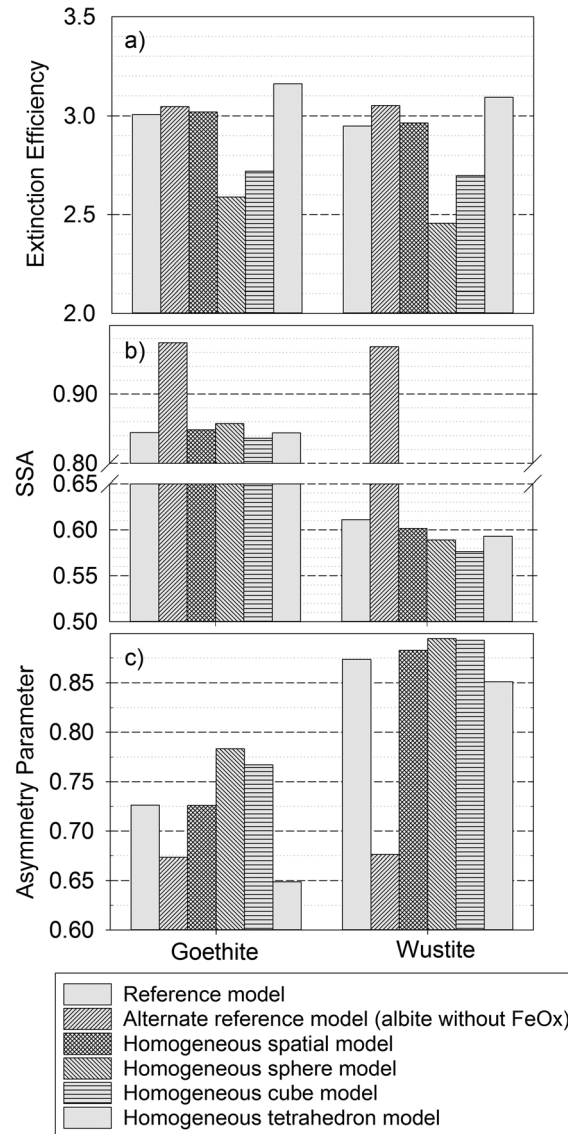


**Figure 6.** Optical properties (a)  $Q_{ext}$ , (b) SSA, and (c)  $\langle \cos \theta \rangle$  for aluminosilicate particle S2 with either goethite or wustite as the iron-containing phase. Incident wavelength is 589 nm.

particles LA3 and S1. That is,  $\langle \cos \theta \rangle$  is larger for the more absorbing wustite (refractive index  $2.42 + 0.64i$ ) versus less absorbing goethite (refractive index  $2.46 + 0.09i$ ). Thus, for the most part test models adequately accounted for the increase in  $\langle \cos \theta \rangle$  as absorption of the iron oxide phase increased.

**3.2.4. Mineral Particles With Spatially Separated Phases (LA4 and S3)**

As noted previously, LA4 and S3 are iron-containing particles with multiple spatially distinct phases. In both particles, the iron-containing phase is modeled as having a refractive index that contrasts sharply with the other phases. Since phases are spatially separated, we also might expect LA4 and S3 to behave different optically from particles that have their phases more integrated. To account for phase separation among the geometric models, we employed a three-sphere heterogeneous model for LA4 and a four-sphere heterogeneous model for S3.

Figure 7 shows  $Q_{ext}$ , SSA, and  $\langle \cos \theta \rangle$  from models for different compositions of the iron-containing phase (phase 3 in Figure 1d) in particle LA4. As observed for other particles,  $Q_{ext}$  from reference models exhibits little variation across the different compositions of the iron-containing phase. Among test models, we might

model as was also observed for particle LA3 with hematite and goethite. We note that in Figure 2 particle S2 has a dihedral angle of approximately  $60^\circ$ , which is close to that of a tetrahedron ( $71.5^\circ$ ). Thus, S2 is closer in shape to a tetrahedron than other particles in this study.

Like particles LA3 and S1, the principal factor affecting SSA of particle S2 is the identity of the iron oxide phase (Figure 6b). SSAs for all test models are close to the respective reference models; however, unlike particles LA3 and S1, S2 contains far less iron oxide. Only 7.1 to 8.9% of the S2 volume is iron oxide, while 77% of the LA3 volume and 96% of the S1 are iron oxide. Thus, even for particles with  $<10\%$  of their volume as light-absorbing iron oxide, test models successfully approximated SSA for particles with different iron oxide compositions.

As mentioned earlier, in addition to the iron oxide inclusion in S2, the albite phase itself likely contained iron oxide, which accounted for 9% of the particle volume. In Figure 6 we include an alternate reference model to show how SSA and other optical properties would be affected if iron oxide was not included in the albite phase. While  $Q_{ext}$  is little affected by this exclusion, SSA would be as much as 58% higher if iron oxide (e.g., wustite) was not included in the albite phase.

Figure 6c shows that for  $\langle \cos \theta \rangle$ , reference models (excluding the alternate model) exhibit the same trend as for

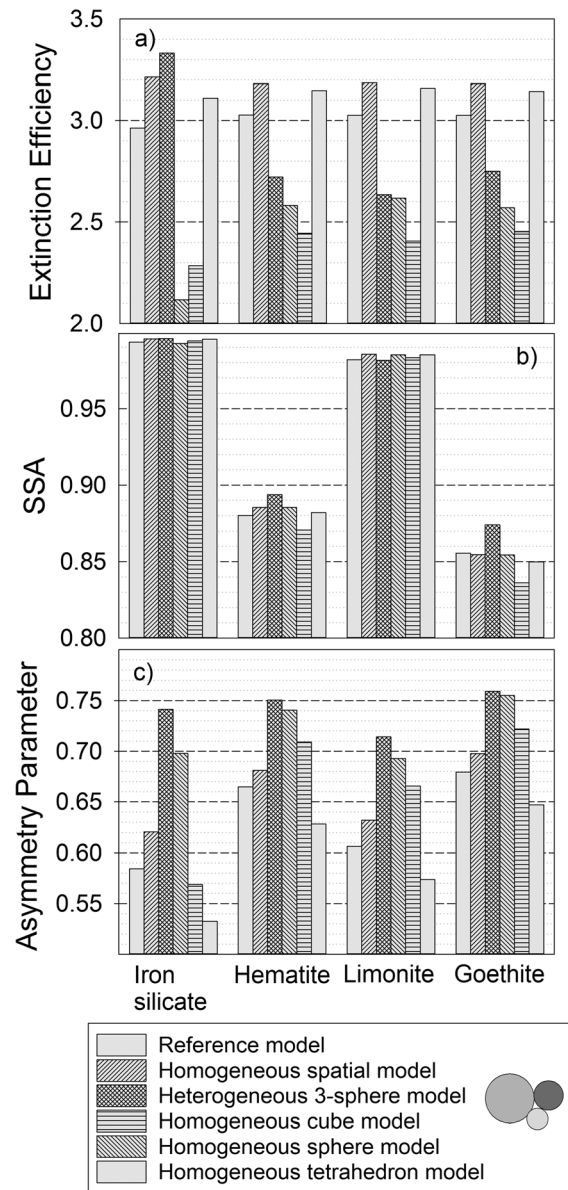


**Figure 7.** Optical properties (a)  $Q_{ext}$ , (b) SSA, and (c)  $\langle \cos \theta \rangle$  for mineral particle LA4 with the iron-containing phase as a silicate, hematite, limonite, or goethite. Incident wavelength is 589 nm.

and  $\langle \cos \theta \rangle$  for the various compositions of the iron oxide phase, which in S3 occupied 24% of the particle volume. Most models exhibit little variation in  $Q_{ext}$  (Figure 8a) among the three compositions of the iron oxide phase. Nevertheless, while  $Q_{ext}$  from the homogeneous spatial model comes closest to the reference model, agreement in the magnitude of  $Q_{ext}$  between the remaining test models and respective reference models is poor. It is noteworthy that in contrast to the other particles, the tetrahedron model for S3 is also unsuccessful at determining  $Q_{ext}$ .

For SSA (Figure 8b), we first note that reference models for particle S3 do not vary substantially with different compositions of the iron oxide phase, in contrast to SSA for particles LA3, LA4, and S1. However, with one exception, test models including the homogeneous spatial model exhibit SSA variation with iron oxide composition that is clearly at odds with the respective reference models. For example, SSA values from the homogeneous spatial and geometric models with highly absorbing wustite are 38 to 41% below the reference model, but  $\leq 3\%$  above the reference model with limonite. In sharp contrast, SSA from the

expect the three-sphere heterogeneous model to best approximate optical properties. However, the three-sphere model overestimates  $Q_{ext}$  when the iron-containing phase is the poorly absorbing iron silicate and underestimates  $Q_{ext}$  when the phase is an absorbing iron oxide. The tetrahedron model in all cases for LA4 comes closest to the respective reference models for  $Q_{ext}$ , varying by  $<5\%$  in all cases, and thus is consistent with other tetrahedron models of particles in this study.

As observed for the other iron-containing particles, SSA (Figure 7b) is largely affected by the identity of the iron-containing phase, which in LA4 occupied 37% of the particle volume. With the phase as almandine/pyrope or as limonite/illite/kaolinite, SSA is  $>0.98$  with all test models in agreement with respective reference models. With the iron phase as the more absorbing hematite/illite/kaolinite mixture or goethite/illite/kaolinite mixture, SSA is  $<0.9$  and more variation exists between the test and reference models.

Compared to SSA, much less agreement between the test and reference models exists for  $\langle \cos \theta \rangle$  (Figure 7c). However, most test models are able to account for variation in  $\langle \cos \theta \rangle$  due to the identity of the iron-containing phase. Nevertheless, it appears that the three-sphere heterogeneous model is least able to account for  $\langle \cos \theta \rangle$  variation.

Optical models of particle S3 present a different picture from other particles in this study. Figure 8 shows  $Q_{ext}$ , SSA,

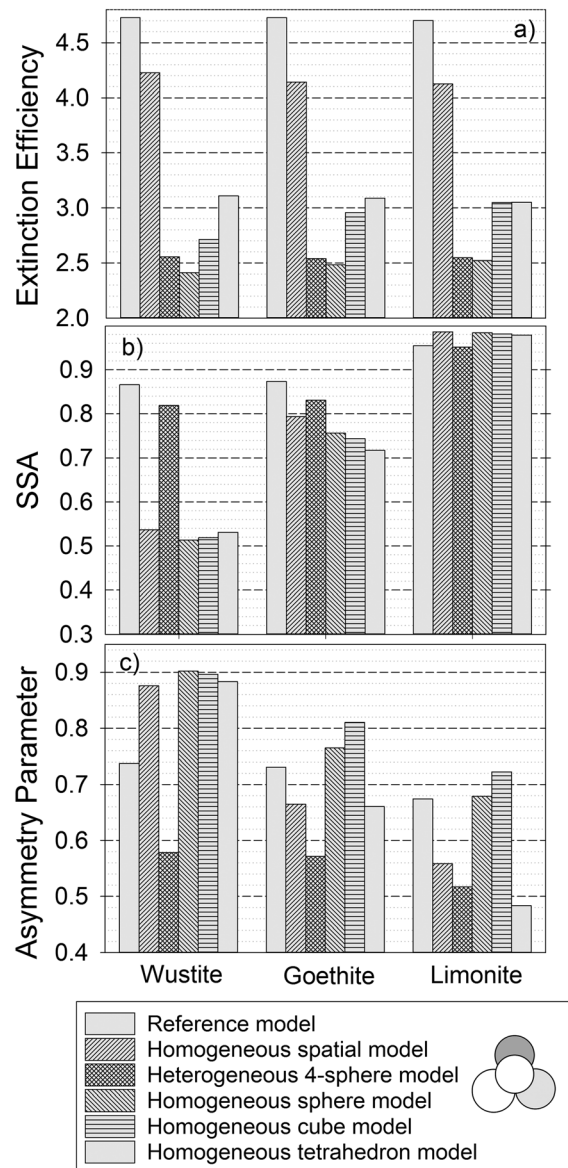


**Figure 8.** Optical properties (a)  $Q_{ext}$ , (b) SSA, and (c)  $\langle \cos \theta \rangle$  for mineral particle S3 with either wustite, goethite, or limonite as the iron-containing phase. Incident wavelength is 589 nm.

Recently, *Adler et al.* [2014] reported that extinction for highly porous aerosols consisting of natural organic matter modeled with DDA was approximately half of the measured extinction for size parameters around 2 to 6. In this case, the discrepancy may have been due in part to the inability of DDA to adjust to rapid changes in the electromagnetic field at phase boundaries, as might occur at the edge of a void within the particle [*Adler et al.*, 2014; *Yurkin and Hoekstra*, 2007].

DDA is most accurate for modeling single spheres and cubes. Error is typically within a few percent when the lattice dispersion method is used to determine particle polarizability [*Yurkin and Hoekstra*, 2007]. For spheres with refractive indexes from 1.6 to 2 and a size parameter of 20, which are parameters closest to those in our study (Table 5), *Yurkin et al.* [2007] determined a relative error of 2 to 6% for  $Q_{ext}$  and 0.7 to 6% for  $\langle \cos \theta \rangle$ .

For irregularly shaped particles, DDA error is expected to be larger than for spheres [*Yurkin and Hoekstra*, 2007; *Yurkin et al.*, 2006]. As a surrogate for irregularly shaped particles in our study, we rely on the comparison by *Xu and Gustafson* [1999] of DDA with an exact analytic solution for the two-sphere aggregate. The Xu

heterogeneous four-sphere model is much closer to reference models. SSA from the four-sphere model is only 5% below the reference model with wustite and <1% below the reference model with limonite.

For  $\langle \cos \theta \rangle$  (Figure 8c), particle S3 also contrasts with the other particles that had a substantial volume for the iron-containing phase. We have noted that the homogeneous spatial model generally approximates  $\langle \cos \theta \rangle$  across different compositions of the iron-containing phase better than other test models. However, for particle S3 the homogeneous spatial model along with the heterogeneous four-sphere model generally performs poorer than the homogenous sphere and cube models.

## 4. Discussion

### 4.1. Sources of Modeling Error

Error in DDA modeling is most often reported in the literature as a relative deviation in the DDA result from an exact nonnumerical solution. This error has most often been examined for spheres by comparing with the classical Mie solution. Nevertheless, discrepancies exist in the assessment of DDA error, which makes error correction difficult. For example, *Flatau et al.* [1993] estimated error at <0.5% for the scattering cross section for a two-sphere aggregate, while *Xu and Gustafson* [1999] estimated error at <10% also for a two-sphere aggregate with similar properties [*Yurkin and Hoekstra*, 2007]. Other errors associated with DDA modeling may need further investigation.

and Gustafson approach was further developed into the generalized multiparticle Mie solution for sphere clusters [Xu, 2003]. As shown in Figure 4 of Xu and Gustafson, relative deviation of the DDA solutions for the extinction efficiency and the asymmetry parameter versus  $|m|kd$  behaves much like a first-order linear function. When the direction of the incident light beam aligns with the axis of symmetry for the two-sphere aggregate ( $k$  symmetry orientation), the relative deviation increases linearly from approximately 1% with  $|m|kd = 0.2$  to 10% with  $|m|kd = 1$ .

An additional source of error in this study is related to the number of steps the particle is rotated in DDSCAT to simulate random orientation. As mentioned in section 2.3, orientation angles  $\Phi$  and  $\beta$  were incremented from  $0^\circ$  to  $360^\circ$  in steps of  $90^\circ$ , while  $\Theta$  was positioned at  $0^\circ$ ,  $90^\circ$ , and  $180^\circ$ , which corresponded to values 1, 0, and  $-1$  of  $\cos(\Theta)$ . The total number of orientations was 48, although some orientations were equivalent. The number of orientations was limited by the length of time for DDSCAT to complete running in some cases. Particle S1 in particular required hundreds of hours.

To test how the number of orientations would affect optical property calculations, we increased the number to 448 for five particle treatments: LA2 with BC, LA3 with hematite, LA4 with goethite, S2 with goethite, and S2 with wustite. To achieve 448 orientations,  $\Phi$  and  $\beta$  were incremented from  $0^\circ$  to  $360^\circ$  in steps of  $45^\circ$ .  $\Theta$  was positioned at  $0^\circ$ ,  $48.2^\circ$ ,  $70.5^\circ$ ,  $90^\circ$ ,  $109.5^\circ$ ,  $131.8^\circ$ , and  $180^\circ$ , which corresponded to values 1, 0.666, 0.333, 0,  $-0.333$ ,  $-0.666$ , and  $-1$  of  $\cos(\Theta)$ .

The deviation in values for  $Q_{\text{ext}}$ ,  $Q_{\text{scat}}$ ,  $\langle \cos \theta \rangle$ , and SSA between 48 and 448 orientations was generally small for the five particle treatments. For the reference models, the maximum deviation among treatments was 5% for  $Q_{\text{ext}}$ , 7% for  $Q_{\text{scat}}$ , 4% for  $\langle \cos \theta \rangle$ , and 2% for SSA. For the heterogeneous geometric models, the maximum deviation was 5% for  $Q_{\text{ext}}$  and  $Q_{\text{scat}}$ , 2% for  $\langle \cos \theta \rangle$ , and 3% for SSA. Among the homogeneous geometric models, the deviation was generally smaller for spheres and tetrahedra than for cubes. For spheres, maximum deviations for  $Q_{\text{ext}}$ ,  $Q_{\text{scat}}$ ,  $\langle \cos \theta \rangle$ , and SSA were within 2%; for tetrahedra maximum deviations were all 4% or less. For cubic models, the maximum deviation was within 5% for  $\langle \cos \theta \rangle$  and SSA but rose to 11% for  $Q_{\text{ext}}$  and 12% for  $Q_{\text{scat}}$ , which was the case for LA4 with goethite. Nevertheless, as Figure 7 shows, an 11% increase in  $Q_{\text{ext}}$  from 2.45 to 2.74 for the cubic model of LA4 with goethite would still have the model performing poorly relative to the reference model.

Other possible sources of error in this study are (1) phase misidentification, (2) use of the Maxwell-Garnett dielectric function for determining the average refractive index in the homogeneous spatial models and homogeneous geometric models, and (3) determination of the volumes of structures in the 3-D spatial model with Avizo. Phase identity is often ambiguous, and phase misidentification is always a possibility. Among the plausible alternatives for the light-absorbing particle phases in this study, phase identification least affected  $Q_{\text{ext}}$ . For the reference models among all particles, variation in the identity of the light-absorbing phase resulted in only a 1.3% variation in  $Q_{\text{ext}}$  on average. Variation in SSA and  $\langle \cos \theta \rangle$  due to the identity of the light-absorbing phase was substantially larger, particularly for the five particles that contained iron. SSA variation in the reference models due to iron-phase identity was 46%, 15%, 27%, 32%, and 10% for particles LA3, LA4, S1, S2, and S3, respectively. Variation in  $\langle \cos \theta \rangle$  for these particles was 42%, 15%, 20%, 18%, and 9%, respectively.

The error associated with the use of the Maxwell-Garnett dielectric function has been shown to depend in part on the size parameter of the individual inclusions ( $x_{\text{inc}}$ ). While it has been assumed that  $x_{\text{inc}} \ll 1$  for the Maxwell-Garnett dielectric function as well for other effective medium approximations, Chylek *et al.* [2000] have shown that Maxwell-Garnett can be applied to particles when  $x_{\text{inc}} \geq 1$ , albeit with resulting larger error. From studies involving DDA, Chylek *et al.* concluded that for  $x_{\text{inc}} \leq 2$ , the error in extinction and scattering cross sections is 10% to 15%. In our study, the particle size parameters ranged from 6.8 to 18 (Table 5). As an approximation, we assume that the size parameter for an individual inclusion was on average one tenth the particle size parameter; thus, we assume that  $x_{\text{inc}}$  ranged from 0.68 to 1.8.

The error associated with volumes of structures in the 3-D model was estimated by assessing the random error in quantifying the area in individual FIB slices assigned to a particular material phase in Avizo, i.e., image segmentation. We assessed the segmentation error as random error by digitally measuring in duplicate the cross-sectional area from five slice images for each particle. The average deviation in the volume of each particle as a sphere was then determined from the duplicate area measurements. Deviations in the volume

determinations among the particles ranged from 1.3% to 5.5%. Deviations in  $Q_{\text{ext}}$ ,  $Q_{\text{sca}}$ ,  $Q_{\text{bkr}}$ , and  $\langle \cos \theta \rangle$  due to segmentation error were then determined for particle LA2 to represent particles with elemental carbon and LA3 to represent particles with light-absorbing iron oxide. Between the carbon-containing particles LA1 and LA2, the latter exhibited the larger relative deviation in volume due to segmentation. Based on LA2, segmentation error in  $Q_{\text{ext}}$ ,  $Q_{\text{sca}}$ , and  $\langle \cos \theta \rangle$  for the carbonaceous particles was negligible,  $<1\%$ . Propagated error in SSA was also  $<1\%$ . Among the particles containing iron (LA3, LA4, S1, S2, and S3), LA3 exhibited the larger relative deviation in volume due to segmentation. Based on LA3, segmentation error in  $Q_{\text{ext}}$ ,  $Q_{\text{sca}}$ , and  $\langle \cos \theta \rangle$  for the iron-containing particles was minimal,  $<5\%$ . Propagated error in SSA was  $\leq 5\%$ .

#### 4.2. Deviation of Test Models From Reference Models

Tables 6–8 show the magnitude of deviation from respective reference models (i.e., absolute deviation) for  $Q_{\text{ext}}$ , SSA, and  $\langle \cos \theta \rangle$  among the various test models and composition treatments. Particle treatments are divided into two groups: (1) where absorption dominated optical behavior and (2) where scattering dominated optical behavior. Here we define absorption as dominant if the imaginary part of the complex refractive index,  $k$ , for the particle as a whole was  $>0.01$ ; scattering as dominant if  $k$  for the particle as a whole was  $<0.01$ .

Tables 6–8 also compare the performance of model types (as the average absolute deviation) between the absorber-dominant and scatterer-dominant particles. While listed in the tables, particle S3 is not included in the table averages. As noted previously and as Tables 6–8 show, the optical behavior of particle S3 is distinctly different from the other iron-containing particles in this study. Factors that may account for this are an exceptionally irregular particle shape due to the loose attachment of phases and a relatively large iron oxide phase alongside highly scattering mineral phases (anorthite, calcite, and gypsum) that are approximately equally in size (Table 4). S3 appears to be the most heterogeneous particle in this study and is, thus, an example of “severe” heterogeneity.

Excluding particle S3, Table 6 shows that the homogeneous spatial models and tetrahedron models performed best on average at approximating  $Q_{\text{ext}}$  ( $<10\%$  from reference models) for both absorber-dominant and scatterer-dominant particles. Less successful are the heterogeneous geometric models, but performance was slightly better for scatterer-dominant particles than for absorber-dominant particles. This is due in part to the poor performance of the core/shell models for the absorber-dominant LA1 and LA2 particles. Results show that for individual particles composition heterogeneity is less important for accurately modeling  $Q_{\text{ext}}$  than particle shape for both absorber-dominant and scatterer-dominant particles. However, shape effects may become less important in modeling  $Q_{\text{ext}}$  (and heterogeneity perhaps more important) for a large population of particles because many distinct particle shapes may appear smoothed for a particle ensemble. In addition, shape effects may become less important over a distribution of sizes for a specific particle shape. We are currently addressing this issue. Nevertheless, while homogeneous spatial models provide a close approximation of a particle’s shape, surface features, and void structure, tetrahedral models may be as successful at modeling  $Q_{\text{ext}}$  because the sharp dihedral angles of the tetrahedron may compensate for a particle’s surface features.

For SSA as shown in Table 7, all models on average performed well ( $<10\%$  of reference models) for all particles except S3. However, we note that while absolute deviation averages in Table 7 are low, dispersions ( $s$ ) are high. As mentioned previously, heterogeneous core-shell models for particles LA1 and LA2 were less successful than other models for these particles and performed worse than heterogeneous geometric models of other particles as well. Table 7 also shows that test models were more successful at approximating SSA for scatterer-dominant particles than for absorber-dominant particles. This is likely due to the difficulty test models had in correctly calculating larger absorption efficiencies for the absorber-dominant particles. All test models successfully approximated SSA for particle S3 when it contained limonite (and was, thus, a scatterer-dominant particle). As mentioned previously, when S3 contained goethite or wustite (and, thus, an absorber-dominant particle), only the heterogeneous four-sphere model successfully approximated SSA.

As mentioned previously, test models were able to exhibit the trend in  $\langle \cos \theta \rangle$ , as well as SSA, with variation in the composition of the iron-containing phase. Table 8 shows that all models for the absorber-dominant particles approximated  $\langle \cos \theta \rangle$  within 10% of reference models on average. For the scatterer-dominant

**Table 6.** Performance of Test Models for Particles Classified as Overall Absorbing or Scattering: Extinction Efficiency

Absorber or Scatterer as Dominant Phase <sup>a</sup>	Particles	Absolute Deviation in $Q_{ext}$ From Reference Models					
		Homogeneous Geometric Model		Heterogeneous Geometric Model		Homogeneous Geometric Models	
		Spatial Model <sup>c</sup>	Type	Sphere	Cube	Tetrahedron	
Absorber dominant	BC; $k = 0.39$ to $0.48$	0.0234 ( $n = 2$ )	Core/shell	0.198 ( $n = 2$ )	0.114 ( $n = 2$ )	0.203 ( $n = 2$ )	0.114 ( $n = 2$ )
	Graphite; $k = 0.72$ to $0.87$	0.0145 ( $n = 2$ )	two spheres	0.216 ( $n = 2$ )	0.107 ( $n = 2$ )	0.192 ( $n = 2$ )	0.0676 ( $n = 2$ )
	Hematite; $k = 0.072$	0.0095	two spheres (LA3)	0.250	0.152	0.275	0.0179
	Goethite; $k = 0.06$ to $0.09$	0.0037 ( $n = 2$ )	two spheres (LA3)	0.160 (LA3)	0.0574 ( $n = 2$ )	0.157 ( $n = 2$ )	0.0746 ( $n = 2$ )
	Wustite; $k = 0.038$	0.0051			0.0856	0.167	0.0489
Average absolute deviation $\pm s$	0.012 $\pm$ 0.010	0.21 $\pm$ 0.04		0.19 $\pm$ 0.06	0.099 $\pm$ 0.055	0.099 $\pm$ 0.055	0.099 $\pm$ 0.055
Scatterer dominant	Goethite; $k = 0.016^b$	( $n = 8$ )	( $n = 6$ )	( $n = 8$ )	( $n = 8$ )	( $n = 8$ )	( $n = 8$ )
	Wustite; $k = 0.112^b$	0.124	four spheres	0.463	0.474	0.474	0.347
		0.106	four spheres	0.459	0.426	0.490	0.342
	Limonite; $k = 0.0032$ to $0.0042$	0.0037 ( $n = 2$ )	two spheres	0.0686 LA3	0.102 ( $n = 2$ )	0.172 ( $n = 2$ )	0.0710 ( $n = 2$ )
	Albite/Gypsum; $k = 0.00073$	0.0044	three spheres		0.0954	0.139	0.0513
	Albite/Almandine/Pyrope/Quartz; $k = 0.00014$	0.0849		0.124	0.229	0.0286	0.0497
	Albite/Ilite/Kaolinite/Quartz; $k = 0.00433$ to $0.00047$	0.0520 ( $n = 3$ )		0.107 ( $n = 3$ )	0.144 ( $n = 3$ )	0.195 ( $n = 3$ )	0.195 ( $n = 3$ )
Average absolute deviation $\pm s$	0.036 $\pm$ 0.032	0.10 $\pm$ 0.02		0.17 $\pm$ 0.06	0.16 $\pm$ 0.08	0.052 $\pm$ 0.038	
Calcite/Anorthite/Gypsum; $k = 0.00073^b$	0.123	four spheres	0.459	0.464	0.352	0.352	

<sup>a</sup>Absorber is dominant if the imaginary part of complex refractive index,  $k$ , for the whole particle is  $>0.01$ . Scatterer is dominant if  $k$  for whole particle is  $<0.01$ .

<sup>b</sup>Treatments for particle S3 (italics) are not included in determinations of the average absolute deviation as explained in text.

<sup>c</sup>Model includes particle shape, surface features, and voids.

**Table 7.** Performance of Test Models for Particles Classified as Overall Absorbing or Scattering: Single Scattering Albedo

Absorber or Scatterer as Dominant Phase <sup>a</sup>	Particle(s)	Absolute Deviation in SSA From Reference Models					
		Homogeneous Spatial Model <sup>c</sup>	Heterogeneous Geometric Model Type	Homogeneous Geometric Models			
			Core/shell	Sphere	Cube	Tetrahedron	
Absorber dominant	BC; $k = 0.39$ to $0.48$	LA1 and LA2	0.0189 ( $n = 2$ )	0.0641 ( $n = 2$ )	0.0220 ( $n = 2$ )	0.0299 ( $n = 2$ )	0.0246 ( $n = 2$ )
	Graphite; $k = 0.72$ to $0.87$	LA1 and LA2	0.0162 ( $n = 2$ )	0.108 ( $n = 2$ )	0.0578 ( $n = 2$ )	0.0923 ( $n = 2$ )	0.0581 ( $n = 2$ )
	Hematite; $k = 0.072$	LA3	0.0264	0.0234	0.0002	0.0408	0.0124
	Goethite; $k = 0.06$ to $0.09$	LA3 and S1	0.0135 ( $n = 2$ )	0.0406 (LA3)	0.0570 ( $n = 2$ )	0.0639 ( $n = 2$ )	0.0339 ( $n = 2$ )
	Wustite; $k = 0.038$	S2	0.0157		0.0362	0.0568	0.0296
	Average Absolute Deviation $\pm s$		0.017 $\pm$ 0.012 ( $n = 8$ )	0.068 $\pm$ 0.035 ( $n = 6$ )	0.039 $\pm$ 0.026 ( $n = 8$ )	0.059 $\pm$ 0.028 ( $n = 8$ )	0.034 $\pm$ 0.019 ( $n = 8$ )
	Goethite; $k = 0.016^b$	S3	0.0914	0.0488	0.133	0.148	0.178
	Wustite; $k = 0.112^b$	S3	0.380	0.0547	0.407	0.401	0.387
	Limonite; $k = 0.0032$ to $0.0042$	LA3 and S1	0.0260 ( $n = 2$ )	0.0090 LA3	0.0603 ( $n = 2$ )	0.120 ( $n = 2$ )	0.035 ( $n = 2$ )
	Albite/Gypsum; $k = 0.00073$	S2	0.0047		0.0153	0.0097	0.00060
Albite/Almandine/Pyrope/Quartz; $k = 0.00014$	LA4	0.0021		0.0010	0.00076	0.0018	
Albite/Ilite/Kaolinite/Quartz; $k = 0.00433$ to $0.00047$	LA4	0.0036 ( $n = 3$ )	three spheres	0.0036 ( $n = 3$ )	0.0116 ( $n = 3$ )	0.0040 ( $n = 3$ )	
Average Absolute Deviation $\pm s$		0.0099 $\pm$ 0.012 ( $n = 7$ )	0.0097 $\pm$ 0.0089 ( $n = 5$ )	0.021 $\pm$ 0.028 ( $n = 7$ )	0.041 $\pm$ 0.072 ( $n = 7$ )	0.012 $\pm$ 0.016 ( $n = 7$ )	
Calcite/Anorthite/Gypsum; $k = 0.00073^b$	S3	0.0332	four spheres	0.0309	0.0282	0.0256	

<sup>a</sup> Absorber is dominant if the imaginary part of complex refractive index,  $k$ , for the whole particle is  $>0.01$ . Scatterer is dominant if  $k$  for whole particle is  $<0.01$ .

<sup>b</sup> Treatments for particle S3 (italics) are not included in determinations of the average absolute deviation as explained in text.

<sup>c</sup> Model includes particle shape, surface features, and voids.

**Table 8.** Performance of Test Models for Particles Classified as Overall Absorbing or Scattering: Asymmetry Parameter

Absorber or Scatterer as Dominant Phase <sup>a</sup>	Particles	Absolute Deviation in $\langle \cos \theta \rangle$ From Reference Models					
		Homogeneous Spatial Model <sup>c</sup>		Heterogeneous Geometric Model		Homogeneous Geometric Models	
		Type	Type	Sphere	Cube	Tetrahedron	
Absorber dominant	BC; $k = 0.39$ to $0.48$	LA1 and LA2	Core/shell	0.0337 ( $n = 2$ )	0.0116 ( $n = 2$ )	0.0315 ( $n = 2$ )	0.0253 ( $n = 2$ )
	Graphite; $k = 0.72$ to $0.87$	LA1 and LA2	two spheres	0.0679 ( $n = 2$ )	0.0219 ( $n = 2$ )	0.0927 ( $n = 2$ )	0.0673 ( $n = 2$ )
	Hematite; $k = 0.072$	LA3	two spheres (LA3)	0.0152	0.0392	0.0271	0.0441
	Goethite; $k = 0.06$ to $0.09$	LA3 and S1	two spheres (LA3)	0.0419 (LA3)	0.0390 ( $n = 2$ )	0.0568 ( $n = 2$ )	0.0503 ( $n = 2$ )
	Wustite; $k = 0.038$	S2		0.0103	0.0242	0.0221	0.0256
	Average Absolute Deviation $\pm s$			0.014 $\pm$ 0.01 ( $n = 8$ )	0.026 $\pm$ 0.013 ( $n = 8$ )	0.051 $\pm$ 0.032 ( $n = 8$ )	0.044 $\pm$ 0.022 ( $n = 8$ )
	Goethite; $k = 0.016^b$	S3	four spheres	0.218	0.0467	0.108	0.0966
	Wustite; $k = 0.112^b$	S3	four spheres	0.216	0.223	0.216	0.197
	Limonite; $k = 0.0032$ to $0.0042$	LA3 and S1	two spheres	0.223 (LA3)	0.174 ( $n = 2$ )	0.163 ( $n = 2$ )	0.158 ( $n = 2$ )
	Scatterer dominant	Albite/Gypsum; $k = 0.00073$	S2			0.0787	0.0564
Albite/Almandine/Pyrope/Quartz; $k = 0.00014$		LA4	three spheres	0.269	0.195	0.0262	0.0882
Albite/Ilite/Kaolinite/Quartz $k = 0.00433$ to $0.00047$		LA4		0.141 ( $n = 3$ )	0.123 ( $n = 3$ )	0.0757 ( $n = 3$ )	0.0522 ( $n = 3$ )
Average Absolute Deviation $\pm s$				0.026 $\pm$ 0.02 ( $n = 7$ )	0.14 $\pm$ 0.07 ( $n = 7$ )	0.091 $\pm$ 0.083 ( $n = 7$ )	0.095 $\pm$ 0.053 ( $n = 7$ )
Calcite/Anorthite/Gypsum; $k = 0.00073^b$		S3	four spheres	0.233	0.0068	0.0720	0.283

<sup>a</sup>Absorber is dominant if the imaginary part of complex refractive index,  $k$ , for the whole particle is  $>0.01$ . Scatterer is dominant if  $k$  for whole particle is  $<0.01$ .  
<sup>b</sup>Treatments for particle S3 (italics) are not included in determinations of the average absolute deviation as explained in text.  
<sup>c</sup>Model includes particle shape, surface features, and voids.

particles, modeling success was more variable. Table 8 also shows that the homogeneous spatial model was more consistent at approximating  $\langle \cos \theta \rangle$  for both absorber-dominant and scatterer-dominant particles. Since the tetrahedron model was not as successful at approximating  $\langle \cos \theta \rangle$  as for SSA or  $Q_{\text{ext}}$ , results suggest that among the optical properties studied here,  $\langle \cos \theta \rangle$  is particularly sensitive to how models represent particle shape. In this regard, models that represent particles with high shape irregularity as collections of spheres such as for particle S3 do not appear to sufficiently model  $\langle \cos \theta \rangle$ .

## 5. Conclusions

We have presented optical properties of individual heterogeneous urban dust particles from Los Angeles and Seattle based on models of varying complexity. Test models were compared to reference models generated from particle 3-D spatial models that were based on high-resolution element mapping in SEM-EDX and FIB tomography, which accurately reconstructed particle shape and heterogeneity. The test models included compositionally homogeneous and compositionally heterogeneous models. Along with simple geometric shape models (sphere, cube, and tetrahedron), compositionally homogeneous models included spatial models based on FIB tomography that closely approximated actual particle shape, surface features, and void structure. Additionally, compositionally heterogeneous models consisted of collections of spheres to represent different particle phases.

Results showed that homogeneous models, particularly the homogeneous spatial and tetrahedral models, provided better accuracy for the extinction efficiency than other models, including geometric models that attempted to account for heterogeneity. Thus, particle shape appears to be a more important factor for determining extinction efficiency in individual heterogeneous particles than distinguishing the separate phases. This rule applies to particles where absorption is dominant and particles where scattering is dominant. As mentioned previously, shape may be a less important factor for a large ensemble of particles, particularly if the particles are small and compact.

For iron-containing heterogeneous particles, the asymmetry parameter and SSA varied with the composition of the iron-containing phase, even if the phase was  $<10\%$  of the particle volume. The homogeneous spatial model, which accounted for particle shape, surface features, and void structure, generally provided a closer approximation to  $\langle \cos \theta \rangle$  across compositions of the iron oxide phase in these particles. Thus, as with  $Q_{\text{ext}}$ , particle morphology is a more important consideration than composition heterogeneity for modeling the asymmetry parameter in heterogeneous particles.

Whether the iron-containing phase in particles was more absorbing or strongly scattering (e.g., as iron-containing silicate), all homogenous and heterogeneous test models in this study successfully determined SSA. However, for particles that exhibit much compositional and optical heterogeneity (i.e., containing loosely held phases with widely varying refractive indexes) only models that account for phase heterogeneity may be sufficient for determining SSA.

While a highly detailed analysis was presented here, this work was limited by the number of urban dust particles and compositional treatments of each particle. Study of additional particles is needed to better understand how geometric models might better approximate optical properties of heterogeneous urban dusts from different regions and as transformed by in-atmosphere aging. In particular, additional particles should be studied to further determine how much complexity is needed in heterogeneous geometric models to adequately approximate optical properties, particularly  $Q_{\text{ext}}$  of dusts that exhibit severe compositional and optical heterogeneity. In addition, further study is needed to determine the effect of individual particle shapes on backscattering, which is important in remote sensing applications.

## References

- Adler, G., C. Haspel, T. Moise, and Y. Rudich (2014), Optical extinction of highly porous aerosol following atmospheric freeze drying, *J. Geophys. Res. Atmos.*, 119, 6768–6787, doi:10.1002/2013JD021314.
- Albrecht, B. A. (1989), Aerosols, Cloud Microphysics, and Fractional Cloudiness, *Science*, 245(4923), 1227–1230.
- Anderson, C. J., and E. B. Hensley (1975), Index of refraction of barium oxide, *J. Appl. Phys.*, 46, 443.
- Anthony, J. W., R. A. Bideaux, K. W. Bladh, and M. C. Nichols (2016), *Handbook of Mineralogy*, Mineralogical Society of America, Chantilly, Va.
- Asano, S., and M. Sato (1980), Light scattering by randomly oriented spheroidal particles, *Appl. Opt.*, 19(6), 962–974.
- Bedidi, A., and B. Cervelle (1993), Light-scattering by spherical particles with hematite and goethite-like optical-properties: Effect of water impregnation, *J. Geophys. Res.*, 98, 11,941–11,952, doi:10.1029/93JB00188.

### Acknowledgments

We thank Gary A. Norris of the U.S. Environmental Protection Agency, Constantinos Sioutas of the Department of Civil and Environmental Engineering, University of Southern California, and Timothy Gould of the Department of Civil and Environmental Engineering, University of Washington, for assistance in sample collection. We also thank former NIST Undergraduate Research Fellow Sean M. Collins and NIST summer student Andrew Obeng for assistance on particle 3-D spatial modeling. Work by D.L. Ortiz-Montalvo was performed while a National Research Council Research Associate at NIST. Supporting data are contained in seven tables in the supporting information. Additional data are available at <https://doi.org/10.18434/M33X0V>.

- Bi, L., and P. Yang (2014), Accurate simulation of the optical properties of atmospheric ice crystals with the invariant imbedding T-matrix method, *J. Quant. Spectrosc. Radiat. Transfer*, *138*, 17–35, doi:10.1016/j.jqsrt.2014.01.013.
- Bohren, C. F., and D. R. Huffman (1983), *Absorption and Scattering of Light by Small Particles*, Wiley-VCH Verlag GmbH & Co. KGaA, Weinheim, Germany.
- Bohren, C. F., and N. C. Wickramasinghe (1977), On the computation of optical properties of heterogeneous grains, *Astrophys. Space Sci.*, *50*(2), 461–472, doi:10.1007/bf00641750.
- Bond, T. C., and R. W. Bergstrom (2006), Light absorption by carbonaceous particles: An investigative review, *Aerosol Sci. Technol.*, *40*, 27–67.
- Buseck, P. R., and M. Posfai (1999), Airborne minerals and related aerosol particles: Effects on climate and the environment, *Proc. Natl. Acad. Sci. U.S.A.*, *96*, 3372–3379.
- Chen, H., V. H. Grassian, L. V. Saraf, and A. Laskin (2013), Chemical imaging analysis of environmental particles using the focused ion beam/scanning electron microscopy technique: Microanalysis insights into atmospheric chemistry of fly ash, *Analyst*, *138*(2), 451–460, doi:10.1039/C2AN36318F.
- Chylek, P., G. Videen, D. J. W. Geldard, J. S. Dobbie, and H. C. W. Tso (2000), Effective medium approximations for heterogeneous particles, in *Light Scattering by Nonspherical Particles, Theory, Measurements, and Applications*, edited by M. I. Mishchenko, J. W. Hovenier, and L. D. Travis, pp. 273–308, Academic Press, San Diego, Calif.
- Conny, J. M. (2013), The internal composition of atmospheric dust particles from focused ion-beam scanning electron microscopy, *Environ. Sci. Technol.*, *47*, 8575–8581.
- Conny, J. M., and G. A. Norris (2011), Scanning electron microanalysis and analytical challenges of mapping elements in urban atmospheric particles, *Environ. Sci. Technol.*, *45*, 7380–7386.
- Conny, J. M., S. M. Collins, and A. A. Herzing (2014), Qualitative multiplatform microanalysis of individual heterogeneous atmospheric particles from high-volume air samples, *Anal. Chem.*, *86*(19), 9709–9716, doi:10.1021/ac5022612.
- Diner, D. J., G. P. Asner, R. Davies, Y. Knyazikhin, J.-P. Muller, A. W. Nolin, B. Pinty, C. B. Schaaf, and J. Stroeve (1999), New directions in Earth observing: Scientific applications of multiangle remote sensing, *Bull. Am. Meteorol. Soc.*, *80*(11), 2209–2228, doi:10.1175/1520-0477(1999)080<2209:NDIEOS>2.0.CO;2.
- Draine, B. T. (2000), The discrete dipole approximation for light scattering by irregular targets, in *Light Scattering by Nonspherical Particles: Theory, Measurements, and Applications*, edited by M. I. Mishchenko, J. W. Hovenier, and L. D. Travis, pp. 131–145, Academic Press, San Diego, Calif.
- Draine, B. T., and P. J. Flatau (1994), Discrete-dipole approximation for scattering calculations, *J. Opt. Soc. Am.*, *11*, 1491–1499.
- Draine, B. T., and P. J. Flatau (2013), User Guide for the Discrete Dipole Approximation Code DDSCAT 7.3.
- Dubovik, O., A. Smirnov, B. N. Holben, M. D. King, Y. J. Kaufman, T. F. Eck, and I. Slutsker (2000), Accuracy assessments of aerosol optical properties retrieved from Aerosol Robotic Network (AERONET) Sun and sky radiance measurements, *J. Geophys. Res.*, *105*, 9806.
- Dubovik, O., B. Holben, T. F. Eck, A. Smirnov, Y. J. Kaufman, M. D. King, D. Tanre, and I. Slutsker (2002), Variability of absorption and optical properties of key aerosol types observed in worldwide locations, *J. Atmos. Sci.*, *59*, 590–608.
- Dubovik, O., et al. (2006), Application of spheroid models to account for aerosol particle nonsphericity in remote sensing of desert dust, *J. Geophys. Res.*, *111*, D11208, doi:10.1029/2005JD006619.
- Ebert, M., S. Weinbruch, A. Rausch, G. Gorzawski, P. Hoffmann, H. Wex, and G. Helas (2002), Complex refractive index of aerosols during LACE 98 as derived from the analysis of individual particles, *J. Geophys. Res.*, *107*(D21), 8121, doi:10.1029/2000JD000195.
- Ebert, M., S. Weinbruch, P. Hoffman, and H. M. Ortner (2004), The chemical composition and complex refractive index of rural and urban influenced aerosols determined by individual particle analysis, *Atmos. Environ.*, *38*, 6531–6545.
- Egan, W. G., and T. W. Hilgeman (1979), *Optical Properties of Inhomogeneous Materials: Applications to Geology, Astronomy, Chemistry, and Engineering*, Academic Press, New York.
- Falkovich, A. H., E. Ganor, Z. Levin, P. Formenti, and Y. Rudich (2001), Chemical and mineralogical analysis of individual mineral dust particles, *J. Geophys. Res.*, *106*, 18,029–18,036.
- Flatau, P. J., K. A. Fuller, and D. W. Mackowski (1993), Scattering by two spheres in contact: Comparisons between discrete-dipole approximation and modal analysis, *Appl. Opt.*, *32*(18), 3302–3305, doi:10.1364/AO.32.003302.
- Gao, Y., and J. R. Anderson (2001), Characteristics of Chinese aerosols determined by individual-particle analysis, *J. Geophys. Res.*, *106*, 18,037–18,045, doi:10.1029/2000JD900725.
- Hansen, J., M. Sato, and R. Ruedy (1997), Radiative forcing and climate response, *J. Geophys. Res.*, *102*, 6831–6864.
- Haywood, J., and O. Boucher (2000), Estimates of the direct and indirect radiative forcing due to tropospheric aerosols: A review, *Rev. Geophys.*, *38*, 513–543, doi:10.1029/1999RG000078.
- Henning, T., H. Begemann, H. Mutschke, and J. Dorschner (1995), Optical properties of oxide dust grains, *Astron. Astrophys. Suppl. Ser.*, *112*, 143–149.
- Hill, S. C., A. C. Hill, and P. W. Barber (1984), Light scattering by size/shape distributions of soil particles and spheroids, *Appl. Opt.*, *23*(7), 1031.
- Hinds, W. C. (1999), *Aerosol Technology: Properties, Behavior, and Measurement of Airborne Particles*, 2nd ed., John Wiley, New York.
- Holben, B. N., et al. (1998), AERONET—A federated instrument network and data archive for aerosol characterization, *Remote Sens. Environ.*, *66*(1), 1–16, doi:10.1016/S0034-4257(98)00031-5.
- Kahn, R., R. West, D. McDonald, B. Rheingans, and M. I. Mishchenko (1997), Sensitivity of multiangle remote sensing observations to aerosol sphericity, *J. Geophys. Res.*, *102*, 16,861–16,870, doi:10.1029/96JD01934.
- Kahnert, M., and A. Kylling (2004), Radiance and flux simulations for mineral dust aerosols: Assessing the error due to using spherical or spheroidal model particles, *J. Geophys. Res.*, *109*, D09203, doi:10.1029/2003JD004318.
- Kalashnikova, O. V., and R. Kahn (2006), Ability of multiangle remote sensing observations to identify and distinguish mineral dust types: 2. Sensitivity over dark water, *J. Geophys. Res.*, *111*, D11207, doi:10.1029/2005JD006756.
- Kalashnikova, O. V., and I. N. Sokolik (2002), Importance of shapes and compositions of wind-blown dust particles for remote sensing at solar wavelengths, *Geophys. Res. Lett.*, *29*(10), 1398, doi:10.1029/2002GL014947.
- Kalashnikova, O. V., and I. N. Sokolik (2004), Modeling the radiative properties of nonspherical soil-derived mineral aerosols, *J. Quant. Spectrosc. Radiat. Transfer*, *87*, 137–166.
- Kandler, K., N. Benker, U. Bundke, E. Cuevas, M. Ebert, P. Knippertz, S. Rodriguez, L. Schutz, and S. Weinbruch (2007), Chemical composition and complex refractive index of Saharan Mineral Dust at Izana, Tenerife (Spain) derived by electron microscopy, *Atmos. Environ.*, *41*(37), 8058–8074, doi:10.1016/j.atmosenv.2007.06.047.
- Kandler, K., et al. (2009), Size distribution, mass concentration, chemical and mineralogical composition and derived optical parameters of the boundary layer aerosol at Tinfou, Morocco, during SAMUM 2006, *Tellus B-Chem. Phys. Meteorol.*, *61*(1), 32–50, doi:10.1111/j.1600-0889.2008.00385.x.

- King, M. D., Y. J. Kaufman, D. Tanré, and T. Nakajima (1999), Remote sensing of tropospheric aerosols from space: Past, present, and future, *Bull. Am. Meteorol. Soc.*, *80*(11), 2229–2259, doi:10.1175/1520-0477(1999)080<2229:RSOTAF>2.0.CO;2.
- Koepke, P., and M. Hess (1988), Scattering functions of tropospheric aerosols: The effects of nonspherical particles, *Appl. Opt.*, *27*(12), 2422–2430, doi:10.1364/AO.27.002422.
- Levin, Z., E. Ganor, and V. Gladstein (1996), The effects of desert particles coated with sulfate on rain formation in the eastern Mediterranean, *J. Appl. Meteorol.*, *35*(9), 1511–1523, doi:10.1175/1520-0450(1996)035<1511:TEODPC>2.0.CO;2.
- Levy, R. C., L. A. Remer, and O. Dubovik (2007), Global aerosol optical properties and application to Moderate Resolution Imaging Spectroradiometer aerosol retrieval over land, *J. Geophys. Res.*, *112*, D13210, doi:10.1029/2006JD007815.
- Lieke, K. I., T. B. Kristensen, U. S. Korsholm, J. H. Sørensen, K. Kandler, S. Weinbruch, D. Ceburnis, J. Ovadnevaite, C. D. O'Dowd, and M. Bilde (2013), Characterization of volcanic ash from the 2011 Grímsvötn eruption by means of single-particle analysis, *Atmos. Environ.*, *79*, 411–420, doi:10.1016/j.atmosenv.2013.06.044.
- Lohmann, U., and J. Feichter (2005), Global indirect aerosol effects: A review, *Atmos. Chem. Phys.*, *5*(3), 715–737, doi:10.5194/acp-5-715-2005.
- Mishchenko, M. I., J. W. Hovenier, W. J. Wiscombe, and L. D. Travis (2000), Overview of scattering by nonspherical particles, in *Light Scattering by Nonspherical Particles: Theory, Measurements, and Applications*, edited by M. I. Mishchenko, J. W. Hovenier, and L. D. Travis, pp. 29–60, Academic Press, San Diego, Calif.
- Mishchenko, M. I., A. A. Lacis, B. E. Carlson, and L. D. Travis (1995), Nonsphericity of dust-like tropospheric aerosols: Implications for aerosol remote sensing and climate modeling, *Geophys. Res. Lett.*, *22*, 1077–1080, doi:10.1029/95GL00798.
- Mishchenko, M. I., L. D. Travis, R. A. Kahn, and R. A. West (1997), Modeling phase functions for dustlike tropospheric aerosols using a shape mixture of randomly oriented polydisperse spheroids, *J. Geophys. Res.*, *102*, 16,831–16,847.
- Myhre, G. (2009), Consistency between satellite-derived and modeled estimates of the direct aerosol effect, *Science*, *325*(5937), 187–190.
- Myhre, G., et al. (2013), Anthropogenic and Natural Radiative Forcing, in *Climate Change 2013: The Physical Science Basis. Contribution of the Working Group I to the Fifth Assessment Report of the Intergovernmental Panel on Climate Change*, edited by T. F. Stocker et al., pp. 659–740, Cambridge Univ. Press, Cambridge, U. K., and New York.
- Nousiainen, T. (2009), Optical modeling of mineral dust particles: A review, *J. Quant. Spectrosc. Radiat. Transfer*, *110*(14–16), 1261–1279, doi:10.1016/j.jqsrt.2009.03.002.
- Reid, J. S., et al. (2003), Comparison of size and morphological measurements of coarse mode dust particles from Africa, *J. Geophys. Res.*, *108*(D19), 8593, doi:10.1029/2002JD002485.
- Remer, L. A., et al. (2005), The MODIS aerosol algorithm, products, and validation, *J. Atmos. Sci.*, *62*, 947–973.
- Satheesh, S. K., and K. Krishna Moorthy (2005), Radiative effects of natural aerosols: A review, *Atmos. Environ.*, *39*(11), 2089–2110, doi:10.1016/j.atmosenv.2004.12.029.
- Sokolik, I. N., and O. B. Toon (1996), Direct radiative forcing by anthropogenic airborne mineral aerosols, *Nature*, *381*, 681–683.
- Sokolik, I. N., and O. B. Toon (1999), Incorporation of mineralogical composition into models of the radiative properties of mineral aerosol from UV to IR wavelengths, *J. Geophys. Res.*, *104*, 9423–9444.
- Stagg, B. J., and T. T. Charalampopoulos (1993), Refractive indices of pyrolytic graphite, amorphous carbon, and flame soot in the temperature range 25° to 600°C, *Cumbust. Flame*, *94*, 381–396.
- Tegen, I., and I. Fung (1995), Contribution to the atmospheric mineral aerosol load from land-surface modification, *J. Geophys. Res.*, *100*, 18,707–18,726.
- Tegen, I., A. A. Lacis, and I. Fung (1996), The influence on climate forcing of mineral aerosols from disturbed soils, *Nature*, *380*, 419–422.
- Thorpe, A., and R. M. Harrison (2008), Sources and properties of non-exhaust particulate matter from road traffic: A review, *Sci. Total Environ.*, *400*, 270–282.
- Toon, O. B., and J. B. Pollack (1976), A global average model of atmospheric aerosols for radiative transfer calculations, *J. Appl. Meteorol.*, *15*, 225–246.
- Toon, O. B., J. B. Pollack, and B. N. Khare (1976), The optical constants of several atmospheric aerosol species: Ammonium sulfate, aluminum oxide, and sodium chloride, *J. Geophys. Res.*, *81*, 5733–5747.
- Twomey, S. (1974), Pollution and the planetary albedo, *Atmos. Environ.*, *8*, 1251–1256.
- Volten, H., O. Muñoz, E. Rol, J. F. Haan, W. Vassen, J. W. Hovenier, K. Muinonen, and T. Nousiainen (2001), Scattering matrices of mineral aerosol particles at 441.6 nm and 632.8 nm, *J. Geophys. Res.*, *106*, 17,375–17,401, doi:10.1029/2001JD900068.
- Wiscombe, W. J., and A. Mugnai (1988), Scattering from nonspherical Chebyshev particles. 2: Means of angular scattering patterns, *Appl. Opt.*, *27*(12), 2405–2421, doi:10.1364/AO.27.002405.
- Xu, Y.-L. (2003), Scattering Mueller matrix of an ensemble of variously shaped small particles, *J. Opt. Soc. Am. A*, *20*(11), 2093–2105, doi:10.1364/JOSAA.20.002093.
- Xu, Y.-L., and B. A. S. Gustafson (1999), Comparison between multisphere light-scattering calculations: Rigorous solution and discrete-dipole approximation, *Astrophys. J.*, *513*(2), 894.
- Yi, B. Q., C. N. Hsu, P. Yang, and S. C. Tsay (2011), Radiative transfer simulation of dust-like aerosols: Uncertainties from particle shape and refractive index, *J. Aerosol Sci.*, *42*(10), 631–644, doi:10.1016/j.jaerosci.2011.06.008.
- Yurkin, M. A., and A. G. Hoekstra (2007), The discrete dipole approximation: An overview and recent developments, *J. Quant. Spectrosc. Radiat. Transfer*, *106*(1–3), 558–589, doi:10.1016/j.jqsrt.2007.01.034.
- Yurkin, M. A., and A. G. Hoekstra (2016), Corrigendum to “The discrete dipole approximation: An overview and recent developments” [J. Quant. Spectrosc. Radiat. Transfer 106 (2007) 558–589], *J. Quant. Spectrosc. Radiat. Transfer*, *171*, 82–83, doi:10.1016/j.jqsrt.2015.11.025.
- Yurkin, M. A., V. P. Maltsev, and A. G. Hoekstra (2006), Convergence of the discrete dipole approximation: I. Theoretical analysis, *J. Opt. Soc. Am. A*, *23*(10), 2578–2591, doi:10.1364/JOSAA.23.002578.
- Yurkin, M. A., V. P. Maltsev, and A. G. Hoekstra (2007), The discrete dipole approximation for simulation of light scattering by particles much larger than the wavelength, *J. Quant. Spectrosc. Radiat. Transfer*, *106*(1–3), 546–557, doi:10.1016/j.jqsrt.2007.01.033.